SIAM J. IMAGING SCIENCES
Vol. 16, No. 4, pp. 2144–2174

Transionospheric Autofocus for Synthetic Aperture Radar*

Mikhail Gilman† and Semyon V. Tsynkov†

Abstract. Turbulent fluctuations of the electron number density in the Earth's ionosphere may hamper the performance of spaceborne synthetic aperture radar (SAR). Previously, we have quantified the extent of the possible degradation of transionospheric SAR images as it depends on the state of the ionosphere and parameters of the SAR instrument. Yet no attempt has been made to mitigate the adverse effect of the ionospheric turbulence. In the current work, we propose a new optimization-based autofocus algorithm that helps correct the turbulence-induced distortions of spaceborne SAR images. Unlike the traditional autofocus procedures available in the literature, the new algorithm allows for the dependence of the phase perturbations of SAR signals not only on slow time but also on the target coordinates. This dependence is central for the analysis of image distortions due to turbulence, but in the case of traditional autofocus where the distortions are due to uncertainties in the antenna position, it is not present.

Key words. synthetic aperture radar, ionosphere, autofocus, optimization

MSC codes. 68U10, 78M50, 94A08, 94A12

DOI. 10.1137/22M153570X

1. Introduction.

Synthetic aperture radar (SAR) illuminates the target with microwaves and builds an image with the help of a digital signal processing algorithm. Typical SAR interrogating waveforms are narrow-band linear frequency modulated pulses. The same antenna emits the pulses and receives the returns, i.e., signals reflected off the target. The antenna is mounted on an overhead platform, such as an airplane or satellite, while the target area is on the ground. The signal processing algorithm applied to the returns takes into account multiple pulses emitted and received by the antenna at a series of its successive positions, called the synthetic aperture. The resulting image approximates the map of backscattering reflectivity of the target at the central frequency (also called the carrier frequency) of the antenna signal. Hence, mathematically, SAR imaging is the solution of an inverse problem of reconstruction of the target reflectivity with the radar returns as the input data.

Phase perturbations in the returns may cause the degradation of a SAR image, e.g., the loss of contrast and/or geometric distortions. The perturbations may be due to the position uncertainty (trajectory errors of the antenna platform) and/or turbulence of the propagation medium. A procedure to correct the trajectory errors is called the SAR autofocus [24, 33, 54]. The autofocus introduces an additional phase-correcting factor into the signal

*Received by the editors November 21, 2022; accepted for publication (in revised form) July 17, 2023; published electronically November 20, 2023.
https://doi.org/10.1137/22M153570X
Funding: This work was funded by the US Air Force Office of Scientific Research (AFOSR) under award FA9550-21-1-0086.
†Department of Mathematics, North Carolina State University, Raleigh, NC 27695 USA (mgilman@ncsu.edu, https://mgilman.math.ncsu.edu, tsynkov@math.ncsu.edu, https://stsynkov.math.ncsu.edu).

processing algorithm. Its phase is taken as the negative of the estimate of the phase error at each position of the antenna. The required phase error estimates are obtained by the analysis of the distorted images, typically in an iterative procedure [24, 54]. Specialized methods for the mitigation of phase distortions are developed for interferometric problems. In these methods, the phase difference between two or more images is directly converted into a measurable quantity, such as the elevation or change of elevation. See, for example, [5, 26, 40, 53] for ionosphere-induced phase distortions in the interferometric pairs or [48, 49, 63] for the motion compensation methods for differential interferometry (DInSAR).

There is, however, a fundamental difference between the nature of phase perturbations due to the antenna motion and those due to the turbulence in the propagation medium. While the trajectory perturbations can be parameterized by one quantity, the expected position of the antenna (called slow time), the perturbations due to turbulence are affected by the properties of the medium on the path of the signal between the antenna and the target. Hence, turbulence-induced perturbations are functions of the slow time and target coordinates. They cannot be represented as a function of the slow time alone.

Therefore, to obtain a phase correction in the case of turbulence, one would need to know the refractive index of the medium averaged along every path connecting the synthetic aperture and the target. Previously [17, 56, 59], we have analyzed a simpler setting that involved a nonturbulent dispersive medium (Earth's ionosphere) and employed probing on two distinct carrier frequencies to derive the required information; see also [18]. In that case, a key parameter to be obtained is the total electron content (TEC) in the ionosphere, which is the electron number density integrated along the vertical direction. If the TEC does not vary in the horizontal direction, then its reconstruction is the reconstruction of one scalar quantity, as compared to the reconstruction of a function of slow time in the case of an autofocus.

Yet the case of a turbulent medium is more difficult, because the main objective of SAR is to solve the inverse problem of reconstruction of the unknown target reflectivity, and to obtain both the reflectivity and phase correction one still relies only on the same data as used for reconstruction of a univariate phase correction term in the framework of the conventional autofocus. One simplification commonly employed for the analysis of turbulence-induced distortions is the linearization with respect to the nonturbulent part of the electron number density; see [18, Chapter 4]. This eliminates the dependence of perturbations on the frequency of the signal. In this work, we introduce the additional simplifying assumptions that help reduce the dimensionality of the problem.

The first simplification is provided by the concept of a phase screen. For an Earth-observing SAR satellite, the phase perturbations are due to the turbulence in the ionospheric plasma. The mean electron number density of the ionospheric plasma has a maximum at a certain altitude, which is lower than the typical orbit of a SAR satellite. It is common to model this density function by a layer of infinitesimal thickness at this altitude [1, 4, 18, 40]. The phase perturbations are then realized by a bivariate function called the screen (or layer) density.

Additionally, we recall that the ionospheric turbulence affects the SAR imaging in azimuth (the coordinate parallel to the orbit) a lot stronger than it affects the imaging in range (the coordinate normal to the orbit); see [18, Chapter 4] and [19]. Therefore, we restrict the analysis in the paper to the case where the reflectivity depends only on one coordinate, the azimuth.

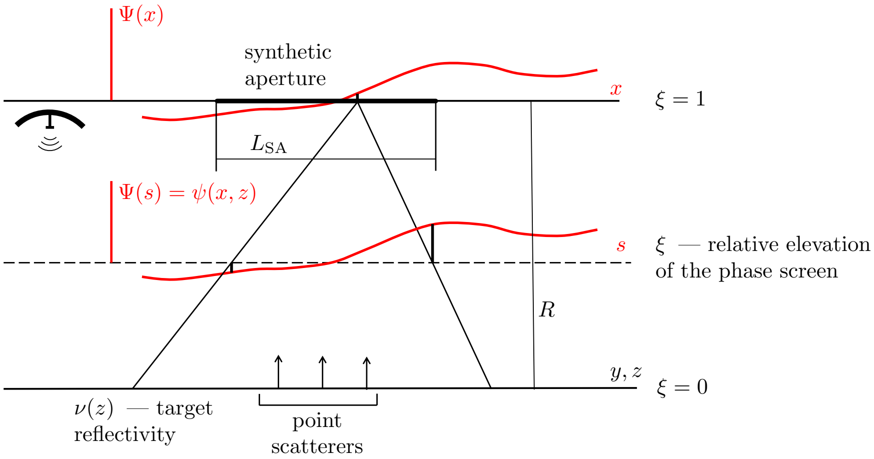

Figure 1. *One-dimensional SAR imaging through a phase screen. The screen density at the relative elevation ξ and phase error due to the antenna position uncertainty are schematically represented by the graph of one and the same univariate function.*

Together with the phase screen assumption, this allows us to represent both unknowns, the target reflectivity and screen density, as univariate functions; see Figure 1. The transition from a full two-dimensional reflectivity to a reflectivity that depends only on one coordinate requires a proper justification. A partial justification of this transition for SAR can be found in [21]. A comprehensive justification will be the subject of a future work.

The phase perturbation function for the geometry shown in Figure 1 is expressed as follows:

$$\begin{gathered} \psi(x,z) = \Psi(s), \\ s \equiv s(x,z) = \xi x + (1-\xi) z, \quad 0 \le \xi \le 1, \end{gathered} \tag{1.1}$$

where ξ is the elevation of the phase screen relative to the orbit altitude, x is the coordinate at the orbit (slow time), z is the azimuthal coordinate of the target, and s is the coordinate along the phase screen. We emphasize that the foregoing simplified formulation still possesses the main feature that distinguishes it from the case of plain trajectory errors: the phase perturbation function ψ in (1.1) depends not only on the slow time but also on the target coordinate.

As a motivating example, we illustrate the role of the phase corrections in SAR signal processing by presenting three simulated one-dimensional images in Figure 2. The target for all three images is composed of three point scatterers represented by δ-functions of equal magnitude.[1] The antenna signals cross through a phase screen with density $\Psi(s)$ at the relative elevation $\xi = 0.5$; see Figure 1. We assume imaging with a low-frequency radar with the carrier frequency of $300 MHz$ corresponding to the wavelength of $1 m$ and the incidence angle $\theta = 60°$ as in [18, Table 1.1]. Note that the level of ionospheric scintillations corresponding to the rms

[1] The definition of a point scatterer for SAR requires care; see [10] or [20, section 3.4].

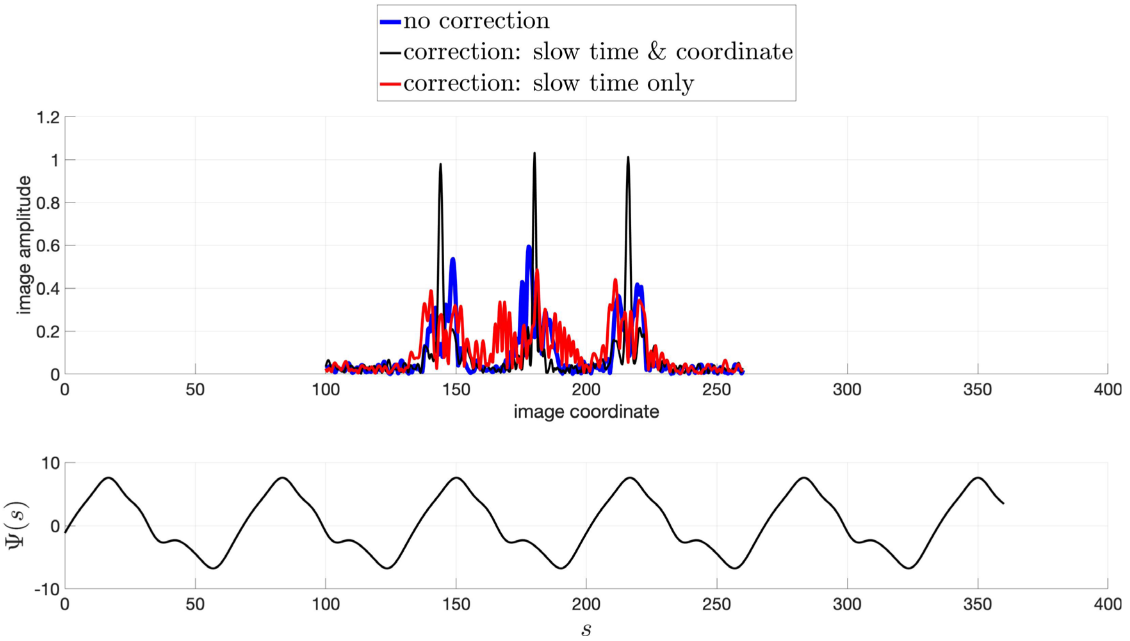

Figure 2. *Examples of one-dimensional SAR images (top plot) in the presence of perturbations due to a phase screen (bottom plot).*

value of Ψ shown in this figure is about $\mathrm{C_k L} \sim 10^{32}\, m^{-2}$, which is a high but not unusual value (see details in Appendix A).

If no phase correction is applied (see subsection 2.2), then the appearance of the peaks that correspond to the point scatterers in the resulting image is rather rugged (blue curve). However, if we apply the correction using the same screen density function that defines the phase perturbations, i.e., $\psi(x,z)$ of (1.1), then the resulting image will display sharp and narrow peaks (black curve). Note that whereas the target consists of point scatterers, the black-colored peaks in Figure 2 have finite width. This width provides a lower bound to the capacity of the SAR instrument to distinguish between closely located targets and is therefore called the SAR resolution. It is finite because the synthetic aperture length is finite. We will show that the black-colored image in Figure 2 is very close to the one we would have obtained if there were no perturbations. Finally, we can use the same screen density function for reconstruction but ignore its dependence on the target coordinate, i.e., take $\psi(x,z) = \Psi(x)$. This case appears similar to that of the antenna trajectory errors where $\xi = 1$. Then, we can see from (1.1) that for each slow time x, the distortions for $z = x$ will be compensated exactly, whereas for other target coordinates (i.e., $z \neq x$), the correction term will not match the perturbation. The resulting image (red curve in Figure 2) does not look much better than the image with no correction at all. This demonstrates the importance of taking into account the geometry of signal propagation.

In our recent work [21], we have developed a procedure of *vertical autofocus* that reconstructs the relative elevation of the phase screen. Our current goal is the full SAR inversion, which is to reconstruct the unknown screen density function $\Psi(s)$, as well as the unknown target reflectivity $\mu(z)$, assuming that the screen elevation ξ is known. The corresponding reconstruction procedure will be called *the transionospheric autofocus.* We will investigate its performance for those transionospheric SAR imaging regimes where the effect of ionospheric turbulence most clearly manifests itself; see [18, Chapter 4] and [19].

The analysis of the various scenarios and parameter estimates relevant for spaceborne SAR imaging and, specifically, imaging through a turbulent ionosphere can be found, e.g., in [18, 19, 41]. In particular, it has been shown that the expected magnitude of turbulent fluctuations may be as high as order one. As the nature of turbulent fluctuations is stochastic, one may see both higher and lower values of phase perturbations for a given level of ionospheric activity. Another important parameter is the spatial (or horizontal) scale of perturbations, which is associated with the correlation length of the turbulent medium. In [18, Chapter 4], we have used the outer scale of turbulence as an estimate of this quantity. For the Earth's ionosphere, the outer scale of turbulence is on the order of kilometers. It has been shown that the imaging regime for which the effect of the ionosphere on spaceborne SAR is most noticeable is where the horizontal scale of perturbations is of the same order or shorter than the synthetic aperture [19]. For a P-band spaceborne SAR instrument with high azimuthal resolution, the latter could be on the order of tens of kilometers [18].

If a short horizontal scale is accompanied by large magnitude of perturbations, then the adverse effect on the image may be severe; see, e.g., [16] and [19, section 4.3.3]. It is a simulated imaging regime of this type that is represented by the blue curve in the top plot of Figure 2. On the other hand, if the horizontal scale appears larger than the length of the synthetic aperture, then the adverse effect of ionospheric turbulence on SAR images reduces significantly [19]. Hereafter, we will be interested in developing an autofocus algorithm capable of mitigating the adverse effect of ionospheric turbulence on SAR images in the case of short-scale perturbations that may have large magnitude.

An excellent starting reference about "plain" SAR autofocus is the book [24]. The more recent and notable developments include the two-dimensional autofocus [37, 54] and the Kalman filter-based real-time autofocus [33] to name a few; see also a recent review in [9]. Additional examples of the optimization-based autofocus include [30, 31, 35]. Another class of methods used to reconstruct ionospheric TEC exploits the effect of Faraday rotation and requires polarimetric SAR imaging. In [27], the ionospheric TEC realized by a phase screen is reconstructed from the polarimetric measurements, and simultaneously, the screen elevation is estimated by means of the parallax between the azimuthal sublooks. A combination of map-drift autofocus and TEC reconstruction using the Faraday rotation is presented in [23]. Note that the effectiveness of the polarimetry-based techniques drops towards the equatorial region where the angle between the Earth's magnetic field and the propagation direction is large, making the Faraday rotation weak. For subsequent references regarding the ionosphere-related autofocus see, e.g., [25, 29, 34].

In the rest of the paper, section 2 presents formulations for the unperturbed SAR (subsection 2.1) and SAR affected by a phase screen (subsection 2.2). The optimization-based approach to transionospheric autofocus is described in section 3. Section 4 presents the numerical simulations for several reconstruction scenarios. We discuss the results and suggest several future research directions in section 5.

2. Problem formulation.

2.1. Imaging without perturbations. For the antenna position $\boldsymbol{x} = (x, R)$, where R is the absolute elevation of the trajectory (see Figure 1), the signal at the target location $\boldsymbol{z} = (z, 0)$ is the retarded potential:

$$u(z,t) = \frac{1}{4\pi} \frac{P(t - |\boldsymbol{x} - \boldsymbol{z}|/c)}{|\boldsymbol{x} - \boldsymbol{z}|}. \tag{2.1}$$

In (2.1), c is the speed of light and $P(t)$ is the antenna waveform that typically is a narrow-band pulse:

$$P(t) = \begin{cases} A(t)\exp(-\mathrm{i}\omega_0 t), & \text{where} \quad \left|\dfrac{1}{A}\dfrac{\mathrm{d}A}{\mathrm{d}t}\right| \ll \omega_0, \quad |t| \le \tau/2, \\ 0 & \qquad\qquad\qquad\qquad\qquad\qquad \text{otherwise.} \end{cases} \tag{2.2}$$

In (2.2), ω_0 is the carrier frequency, and τ is the pulse duration.

Hereafter, we assume that the target is approximately at the broadside of the antenna and the size of the target and that of the synthetic aperture is much smaller than R. Then,

$$|\boldsymbol{x} - \boldsymbol{z}| \approx R + \frac{(x-z)^2}{2R}. \tag{2.3}$$

For the denominator in (2.1), we will keep only the first term of the expansion (2.3), whereas both terms will be used for the oscillating waveform $P(t)$.

Under the first Born approximation, each point of the target is considered a secondary source, so that the signal received by the same antenna is

$$v(x,t) = \int_{\substack{\text{antenna}\\\text{footprint}}} P(t - 2|\boldsymbol{x} - \boldsymbol{z}|/c)\nu(z)\,\mathrm{d}z, \tag{2.4}$$

where $\nu(z)$ is the target reflectivity. We assume that the synthetic aperture and the antenna footprint have the same linear dimension L_{SA} [18, Chapter 2], so that for a given x, the footprint, i.e., the domain of integration in (2.4), is defined as

$$\{z \mid |x - z| \le L_{\text{SA}}/2\}. \tag{2.5}$$

The goal of SAR is to invert (2.4), i.e., find ν given v. This is achieved via SAR signal processing, which includes the application of a matched filter and integration along the synthetic array. Namely, the image $I = I(y)$ at the location $\boldsymbol{y} = (y, 0)$ on the ground (see Figure 1) is given by

$$I(y) = \iint_{\substack{\text{domain of}\\\text{dependence}}} \overline{P(t - |\boldsymbol{x} - \boldsymbol{y}|/c)}\, w(x,y) v(x,t)\,\mathrm{d}t\,\mathrm{d}x = \int W(y,z)\nu(z)\,\mathrm{d}z, \tag{2.6}$$

where the overbar denotes complex conjugate and $w(x,y)$ is a windowing function. The domain of dependence in the first integral on the right-hand side of (2.6) is chosen similarly to (2.5), i.e., for a given y,

$$\{x \mid |x - y| \le L_{\text{SA}}/2\},$$

and the integration in t is performed over the interval where $P(\,\cdot\,)$ is nonzero; see (2.2).[2] The second integral in (2.6) is obtained by substituting $v(x,t)$ into the form of (2.4) and changing the order of integration. Then, the integration with respect to z in the second integral of (2.6) is to be performed over the entire real axis. Accordingly, the expression for the imaging kernel $W(y,z)$ becomes

$$W(y,z) = \iint_{\substack{\{|x-y|\le L_{\mathrm{SA}}/2\}\\ \cap\{|x-z|\le L_{\mathrm{SA}}/2\}}} P(t-2|\boldsymbol{x}-\boldsymbol{z}|/c)\overline{P(t-|\boldsymbol{x}-\boldsymbol{y}|/c)}w(x,y)\,\mathrm{d}x\,\mathrm{d}t. \tag{2.7}$$

We will use either a rectangular or a parabolic windowing function in (2.6):

$$w^{\mathrm{rect}}(x,y) = \begin{cases} 1 & \text{if} \quad |x-y|\le L_{\mathrm{SA}}/2,\\ 0 & \text{otherwise,}\end{cases} \tag{2.8a}$$

$$w^{\mathrm{parab}}(x,y) = w^{\mathrm{rect}}(x,y)\left[1-4\left(\frac{x-y}{L_{\mathrm{SA}}}\right)^2\right]. \tag{2.8b}$$

In the case of $w=w^{\mathrm{rect}}$, the absolute value of $W(y,z)$ given by (2.7) is maximal for $y=z$; see, e.g., [18, section 2.4.4]. Hence, the largest contribution into $I(y)$ comes from $\nu(y)$; see (2.6). For an imaging operator $\nu\mapsto I$ (see (2.6)), this is a desirable property.

The sharpness of the image (resolution) is determined by how quickly the value of $|W(y,z)|$ decreases from its maximum at $y=z$ as $|y-z|$ increases. For the rectangular window (2.8a), substituting (2.2) and (2.3) into (2.7) and dropping the inessential constant factors yields [10, 18]

$$W(y,z)\approx \operatorname{sinc}\left(\pi\frac{y-z}{\Delta_{\mathrm{A}}}\right), \quad \text{where} \quad \Delta_{\mathrm{A}} = \frac{\pi R c}{\omega_0 L_{\mathrm{SA}}}. \tag{2.9}$$

The azimuthal resolution Δ_{A} is the width of the peak in the image of a point scatterer $\nu(z)\sim\delta(z-z_0)$. Such an image is sometimes called the point spread function (PSF). Usually $\Delta_{\mathrm{A}}\ll L_{\mathrm{SA}}$, and formula (2.9) is accurate for $|y-z|\lesssim\Delta_{\mathrm{A}}\ll L_{\mathrm{SA}}$. It can be seen from the expression for the integration domain in (2.7) that $W\equiv 0$ if $|y-z|\ge L_{\mathrm{SA}}$. For parabolic or other windowing functions, the width of the PSF peak will differ from Δ_{A} given by (2.9) by a factor of order one.

2.2. Imaging with perturbations. We will represent the phase perturbations accumulated during the signal round trip between the antenna and the target by a factor $\exp(-\mathrm{i}\psi(x,z))$ (see (1.1)), so that instead of (2.4) the received field becomes

$$v(x,t) = \int_{|x-z|\le L_{\mathrm{SA}}/2} P(t-2|\boldsymbol{x}-\boldsymbol{z}|/c)\exp(-\mathrm{i}\psi(x,z))\nu(z)\,\mathrm{d}z. \tag{2.10}$$

In the case of a transionospheric radar, the perturbations are due to the turbulence in the ionospheric plasma. Formula (2.10) is a result of linearization with respect to the state of the plasma with no turbulence. In particular, the perturbation phase is considered independent of the signal frequency. In addition, in the linearized framework we do not take into account the difference between the average signal propagation speed and speed of light [18, 19].

[2] In practice, the integral over the fast time t may also involve windowing.

The goal of SAR imaging remains the same as that in subsection 2.1: to invert (2.10), i.e., find ν given v. However, as v in (2.10) is "contaminated" with ψ, one also needs a phase correction. Our approach to correcting the phase perturbations in (2.10) is based on the same idea of canceling the oscillations as that in formulae (2.6) and (2.7). In particular, we introduce a phase correction term ψ^{rec} into the reconstruction formula (2.6):

$$I_\psi(y) = \iint_{|x-z|\le L_{\mathrm{SA}}/2} \overline{P(t-|\boldsymbol{x}-\boldsymbol{y}|/c)}\, w(x,y)\exp\left(\mathrm{i}\psi^{\mathrm{rec}}(x,y)\right) v(x,t)\,\mathrm{d}t\,\mathrm{d}x. \tag{2.11}$$

This leads to the following representation of the image:

$$I_\psi(y) = \int W_\psi(y,z)\nu(z)\,\mathrm{d}z, \tag{2.12}$$

where the new imaging kernel is given by

$$\begin{aligned} W_\psi(y,z) = \iint_{\substack{\{|x-y|\le L_{\mathrm{SA}}/2\}\\ \cap\{|x-z|\le L_{\mathrm{SA}}/2\}}} & P(t-2|\boldsymbol{x}-\boldsymbol{z}|/c)\overline{P(t-|\boldsymbol{x}-\boldsymbol{y}|/c)} \\ & \cdot w(x,y)\exp\left(\mathrm{i}\psi^{\mathrm{rec}}(x,y)-\mathrm{i}\psi(x,z)\right)\mathrm{d}x\,\mathrm{d}t. \end{aligned}$$

Using formula (2.3) and choosing a rectangular window, we obtain

$$W_\psi(y,z) \approx \int_{\substack{\{|x-y|\le L_{\mathrm{SA}}/2\}\\ \cap\{|x-z|\le L_{\mathrm{SA}}/2\}}} \exp\left[\mathrm{i}\underbrace{\frac{2\omega_0}{Rc}(y-z)\left(x-\frac{y+z}{2}\right)}_{\text{term }\mathbf{A}} + \mathrm{i}\underbrace{\left(\psi^{\mathrm{rec}}(x,y)-\psi(x,z)\right)}_{\text{term }\mathbf{B}}\right]\mathrm{d}x. \tag{2.13}$$

If $\psi(x,z)$ is known, then the choice of $\psi^{\mathrm{rec}}(x,y)=\psi(x,y)$ maximizes $W_\psi(y,z)$ for $y=z$, which is desirable. For $y\ne z$, we will assess the effect of the additional term $\mathbf{B}$ in the exponent on the right-hand side of (2.13) when the function $\psi^{\mathrm{rec}}=\psi$ is realized via the phase screen model (1.1), the relative screen elevation ξ is not too close to either 0 or 1, the function Ψ is smooth, and its horizontal scale L_Ψ satisfies $L_\Psi \gg \Delta_{\mathrm{A}}$.[3] In particular:

- For $|y-z|\lesssim \Delta_{\mathrm{A}}$, we can use the following expansion:

  $$|\psi^{\mathrm{rec}}(x,y)-\psi(x,z)| \equiv |\psi(x,y)-\psi(x,z)| \approx |(1-\xi)\Psi'(s(x,z))\cdot(y-z)| \sim (1-\xi)\frac{\|\Psi\|}{L_\Psi}|y-z|.$$

  Then, we can see that the term $\mathbf{B}$ in (2.13) can be ignored as long as

  $$(1-\xi)\frac{\|\Psi\|}{L_\Psi}\Delta_{\mathrm{A}} \ll 1. \tag{2.14}$$

  Given that $\Delta_{\mathrm{A}}/L_\Psi \ll 1$, we can expect this condition to be satisfied even when $\|\Psi\|\sim 1$, i.e., the magnitude of the phase perturbations per se is not small.
- For $|y-z|\gg\Delta_{\mathrm{A}}$, the phase of the integrand in (2.13) oscillates due to the term $\mathbf{A}$ with or without the term $\mathbf{B}$. Hence, $|W|$ becomes small compared to its peak value at $y=z$, similar to (2.9).

[3]The latter assumption is quite reasonable: the resolution of the Earth-observing SAR instruments is typically less than $50m$ [43].

Altogether, we find that the correction of phase perturbations restores the quality of the image, as demonstrated by the black curves in the top plot of Figure 2. However, this correction requires that the perturbation function ψ be known at the time of image acquisition. In practice, this is usually not the case. Hence, our goal is to reconstruct the perturbation from the available data, i.e., the received signal $v(x,t)$.

2.3. Governing equations. The procedure of range compression described in [21] allows one to extract and, subsequently, drop the time-dependent terms in (2.10) and (2.11) after formula (2.3) has been used for distances. Introduce the nondimensional aperture length $F = L_{\mathrm{SA}}/\Delta_{\mathrm{A}} \gg 1$ and consider the coordinates x, y, z, and s normalized by Δ_{A}, which also makes them dimensionless. Then, the reflectivity $\mu(z)$, received signal $u(x)$, and SAR image $\mathcal{I}(y)$ are (cf. formulae (2.10) and (2.11))

$$u(x) = \int_{x-F/2}^{x+F/2} \exp\left(\mathrm{i}\pi(x-z)^2/F\right) \exp\left(-\mathrm{i}\psi(x,z)\right)\mu(z)\,\mathrm{d}z, \tag{2.15}$$

$$\mathcal{I}(y) = \int_{y-F/2}^{y+F/2} \exp\left(-\mathrm{i}\pi(x-y)^2/F\right) \exp\left(\mathrm{i}\psi^{\mathrm{rec}}(x,y)\right)w(x,y)u(x)\,\mathrm{d}x, \tag{2.16}$$

where $\psi(x,z)$ and $\psi^{\mathrm{rec}}(x,y)$ are expressed via the actual screen density $\Psi(s)$ and reconstruction density $\Psi^{\mathrm{rec}}(s)$, respectively, using formula (1.1) with ξ considered a known constant.[4] Similar to (2.12), there is a convolution-type relation between the image and reflectivity that can be derived from (2.15) and (2.16):

$$\mathcal{I}(y) = \int W_\psi(y,z)\mu(z)\,\mathrm{d}z,$$

where W_ψ is still given by (2.13).

3. Optimization approach to autofocus.

3.1. Solution of inverse problem versus autofocus. Equation (2.15) is a model that defines the received radar signal u via the target reflectivity μ and phase perturbation ψ. It allows one to formulate the problem of SAR imaging, i.e., the inverse problem of obtaining the unknown μ for a given u, which represents the data. In doing so, as the perturbation phase ψ directly affects u as well, it needs to be reconstructed along with μ or compensated for.

Equation (2.16) renders an approximate inversion of (2.15) in the sense that the image $\mathcal{I}$ approximates the unknown reflectivity μ. The inversion (2.16) is convenient to implement because it is defined as a direct operation, via the integration along the synthetic array. Its primary deficiency in the case of transionospheric imaging is that it requires the reconstruction phase ψ^{rec} that cannot, generally speaking, be assumed to be known.

Therefore, one may consider a general inverse problem where both μ and ψ are reconstructed by minimizing an appropriately chosen measure of discrepancy between the model signal u of (2.15) and the observed signal u_{observed}, which represents the data:

[4]The relative screen elevation ξ can be thought of as obtained with the help of the vertical autofocus [21].

$$\|u - u_{\text{observed}}\| \to \min. \tag{3.1}$$

The minimization in (3.1) is carried through by varying μ and ψ that define u via (2.15), while u_{observed} is given. The final reconstructed μ and ψ are those that render the minimum.

One can think of a broad variety of the concrete optimization formulations that realize (3.1). Regardless of the specific detail, though, a common concern is the potential ill-posedness. Indeed, (2.15) contains a convolution, and deconvolution operators are often ill-posed [60]. This means that if the observed data u_{observed} are noisy,

$$u_{\text{observed}}(x) = u_{\text{true}}(x) + u_{\text{noise}}(x), \tag{3.2a}$$

then the noise component may get amplified in the process of inversion. In formula (3.2a), u_{true} denotes the true signal that corresponds to substituting the actual unknown μ and ψ into (2.15). In that regard, the direct inversion (2.16) offers another advantage. If applied to plain SAR imaging with no ionosphere and no phase correction, it provides the best L_2 signal-to-noise ratio when reconstructing from noisy data [11, section 4.1].

In addition to the data being noisy, the reflectivity μ is often subject to clutter:

$$\mu(z) = \mu_{\text{target}}(z) + \mu_{\text{clutter}}(z). \tag{3.2b}$$

Clutter may obscure the true target. For example, a target composed of a number of point scatterers (see, e.g., Figure 2) can be parameterized by their locations z_m and amplitudes b_m, $m = 1, \ldots, M$:

$$\mu_{\text{target}}(z) = \sum_{m=1}^{M} b_m \delta(z - z_m). \tag{3.3}$$

In this case, the set $\{(b_m, z_m)\}$ provides a low-dimensional parameterization of the target reflectivity function. However, the clutter term in (3.2b) gets in the way of describing the target using a small number of parameters, which is important for optimization (3.1).

Given the potential hurdles presented by (3.2) for the general variational inversion (3.1), as well as the advantages of direct inversion (2.16) in terms of both its algorithmic simplicity and reduced ill-posedness, in the current work we use the direct inversion. Then, the key issue is how to define the reconstruction phase ψ^{rec} for (2.16). To address this issue, we introduce the algorithm of transionospheric autofocus.

In transionospheric autofocus, we choose a certain metric of $\mathcal{I}(y) \equiv \mathcal{I}(y, \psi^{\text{rec}})$ and optimize it by varying ψ^{rec}:

$$\|\mathcal{I}(y, \psi^{\text{rec}})\| \to \min. \tag{3.4}$$

One can consider various cost functions $\|\cdot\|$ for minimization (3.4). In subsection 3.2, we use a discrete counterpart of the L_4 norm. Otherwise, if the target contains a point scatterer, one may think of increasing the height of the peak and/or making the peak as narrow as possible. Then, the standard imaging performance metrics, such as the peak-to-sidelobe ratio (PSLR) or integrated sidelobe ratio (ISLR) [13], can be employed.

A fundamental difference between the minimization (3.1) and (3.4) is that whereas (3.1) can be interpreted as fitting the observed data u_{observed} by choosing the appropriate μ and ψ, the autofocus (3.4) is not a data fitting approach. The data are substituted into (2.16) directly, while the minimization (3.4) determines the best ψ^{rec} as the one that optimizes the specific desired characteristics of the resulting image $\mathcal{I}(y, \psi^{\text{rec}})$.

3.2. Numerical model. The ionospheric screen density functions $\Psi(s)$ and $\Psi^{\text{rec}}(s)$ that define $\psi(x,z)$ and $\psi^{\text{rec}}(x,y)$, respectively, via (1.1), should be random,[5] yet their spectrum should be specified according to the observed spectrum of ionospheric perturbations; see, e.g., [7, 52]. We will mention here two noteworthy approaches to doing so (for a more detailed discussion, see [8]). One option (see, e.g., [2, 7]) is to process the white noise with a filter such that the output has the desired spectral characteristics. An alternative option, employed by [6, 22, 46], is to represent $\Psi(s)$ as a finite sum of Fourier harmonics:

$$\begin{aligned} \Psi(s) &= \operatorname{Re} \sum_{n=1}^{N} a_n \exp\left(\mathrm{i} k_n s + \mathrm{i}\varphi_n\right) \\ &= \sum_{n=1}^{N} \left(p_n \cos(k_n s) + q_n \sin(k_n s)\right), \end{aligned} \tag{3.5}$$

where $a_n, k_n \in \mathbb{R}_+$ and $\varphi_n, p_n, q_n \in \mathbb{R}$. The choice of $\{(a_n, k_n)\}$ defines the spectrum of the simulated phase screen, whereas the phases φ_n are independent identically distributed random numbers with uniform distribution over $(0, 2\pi)$. For this work, we choose the latter option because it specifies the phase screen with a small number of parameters. Note that keeping the number of control variables low is critically important for the effectiveness of optimization procedures.

We construct the wavenumbers for (3.5) according to

$$k_n = n \frac{2\pi}{(l_{\max}/\Delta_{\mathrm{A}})}, \tag{3.6}$$

where the longest period of perturbations $l_{\max}$ is a parameter of the problem. This parameter characterizes the horizontal scale of perturbations in our model of ionospheric turbulence. Note that even when the spectrum in (3.5) and (3.6) is fixed, any individual realization of the phase screen still depends on the set of phases $\{\varphi_n\}$. It should also be mentioned that modern SAR satellites, such as TerraSAR-X, can produce stripmap images with the azimuthal extent of $50km$ (and acquisition length extendable to over $10^3 km;$ see [57]), which is larger than the outer scale of turbulence. At the same time, it has been found that phase perturbations with the scales over L_{SA} have little effect on SAR images; see [19]. Hence, it does not make sense to use $l_{\max} \gg L_{\mathrm{SA}}$ in (3.6).

In addition, we define the magnitude of perturbations a_s as the L_2 norm of Ψ in (3.5):

$$a_s = \left(\sum_n a_n^2\right)^{1/2}. \tag{3.7}$$

The magnitude of perturbations is a key quantity that affects the distortions of SAR images.

[5]At least, the procedure of building these functions should be capable of producing multiple realizations.

The reconstruction density is represented similarly to (3.5):

$$\Psi^{\mathrm{rec}}(s) = \sum_{n=1}^{N^{\mathrm{rec}}} \left(p_n^{\mathrm{rec}} \cos(k_n^{\mathrm{rec}} s) + q_n^{\mathrm{rec}} \sin(k_n^{\mathrm{rec}} s)\right). \tag{3.8}$$

For the minimization (3.4) that implements autofocus, the optimization variables in (3.8) will be p_n^{rec} and q_n^{rec}. The reconstruction wavenumbers k_n^{rec}, as well as their total number N^{rec} in (3.8), can be chosen differently from those in (3.5). The motivation for doing so is to avoid committing the so-called *inverse crime* [12, section 5.3]. The latter refers to the parameterization of an inverse problem in such a way that the resulting finite set of equations over a finite set of unknowns would have an exact solution. Independently, the introduction of the noise term into the data (see (3.2a)) contributes along the same lines.

The noise term in formula (3.2a) is realized as follows:

$$u_{\mathrm{noise}} = a_{\mathrm{noise}} \cdot \left(\frac{1}{2}\right)^{1/2} \cdot \max(|u(x)|) \cdot n_{\mathrm{compl}}, \tag{3.9}$$

where $a_{\mathrm{noise}} = 0.05$ and the real and imaginary parts of n_{compl} are arrays of independent standard normal Gaussian variables of the appropriate dimension. The dimension is equal to that of the discretization of quadratures in formulae (2.15) and (2.16) (see section 4). The noise term (3.9) is added when u computed according to (2.15) is substituted into (2.16).

The clutter term in formula (3.2b) is realized via the speckle model [47]:

$$\mu_{\mathrm{clutter}} = a_{\mathrm{clutter}} \cdot \left(\frac{d}{2}\right)^{1/2} \cdot n_{\mathrm{compl}}, \tag{3.10}$$

where $a_{\mathrm{clutter}} = 0.1$ and n_{compl} is the same as that used in (3.9). The reflectivity μ given by (3.2b), (3.3), and (3.10) is substituted under the integral in (2.15) that yields the reflected signal u.

Altogether, there are three instances where the model parameters are generated randomly:

- The phases $\{\varphi_n\}$ in the Fourier representation (3.5) of the phase screen density $\Psi(s)$: one random number for each n.
- The term n_{compl} in the expression for noise (3.9): two random numbers (the real and imaginary parts) for each discrete location x.
- The term n_{compl} in the expression for clutter (3.10): two random numbers (the real and imaginary parts) for each discrete location z.

In the numerical simulations of section 4, we use one specific realization of the set of random variables $(\{\varphi_n\}, \mu_{\mathrm{clutter}}, u_{\mathrm{noise}})$ for all our experiments except those discussed in subsection 4.2.5 and Appendix C. For the former, we use 10 different realizations of $(\{\varphi_n\}, \mu_{\mathrm{clutter}}, u_{\mathrm{noise}})$. For the latter, we generate 30 realizations, and also the sets $\{(b_m, z_m)\}$ in (3.3) vary from one realization to another (see the details in Appendix C).

Finally, we consider a cost function as negative of the fourth power of the ℓ_4 norm of the discretized image $\mathcal{I}$ defined by (2.16):

$$\mathrm{Cost}[\Psi^{\mathrm{rec}}] = -\sum_j |\mathcal{I}(y_j, \Psi^{\mathrm{rec}})|^4, \tag{3.11}$$

where y_j are the sampling points. A theoretical justification for using the cost function (3.11) has been given in [44] for the case of a traditional autofocus, i.e., $\xi = 1$ in (1.1), for two-dimensional images and spotlight processing.[6] A wider class of cost functions including those based on ℓ_p metrics has been introduced and analyzed in [45] for the problem of adaptive optics described by the Fresnel–Kirchhoff equation that is similar to the spotlight case in SAR. In [15] (see also [58]), we can find a numerical study for the cost functions given by $-\sum_j |\mathcal{I}(y_j)|^{2\beta}$ with different values of β and different types of targets. It was found that the cost function with large β (in particular, $\beta = 5$) is efficient when there are very bright isolated pixels but fails once the contrast drops. At the same time, small β (such as $\beta = 0.5$) works well when there are large dark regions (in SAR imagery, this may correspond to reflection from a lake or freshly paved surface) but poorly for bright scatterers on top of the clutter. The case of $\beta = 2$ that corresponds to (3.11) is the one most frequently used, apparently because of its universality.

In addition to the ℓ_p metric with $p = 4$ that corresponds to (3.11), we have conducted numerical experiments for other values of p, including the well-known sparsity-promoting metric $p = 1$. The demonstrated performance was found inferior to (3.11). Other potential cost functions include the traditional metrics used to assess the PSF quality, e.g., ISLR or PSLR [13]. They could be effective when strong point scatterers are present. However, gradient-based optimizers work well if the cost function is a smooth function of the optimization variables. For the metrics such as ISLR or PSLR smoothness is not guaranteed though because the peak location (i.e., $\arg\max_y |\mathcal{I}(y, \Psi^{\rm rec})|$) does not necessarily depend continuously on the optimization variables. This appears to be the case when the optimization variables are $p_n^{\rm rec}$ and $q_n^{\rm rec}$ in (3.8). Therefore, we did not use PSLR or ISLR in this work. On the other hand, the metric (3.11) is a continuous function of $p_n^{\rm rec}$ and $q_n^{\rm rec}$. Moreover, unlike the ℓ_1-norm, it is smooth with respect to these optimization variables, as one can see by substituting (3.5) and (1.1) into (2.16).

The formulation for the cost function (3.11) may also be extended by incorporating a regularization term. Regularization terms enforce certain a priori properties on the set of control variables. In our case, we want the amplitudes of harmonics of the resulting phase screen function $\Psi^{\rm rec}(s)$ to decrease as the wavenumber increases. Hence, we add a penalty proportional to $\|\Psi'\|_2^2$. The final form of the cost function used in the numerical experiments is as follows:

$$\text{Cost}[\Psi^{\rm rec}] = -d\sum_j |\mathcal{I}(y_j, \Psi^{\rm rec})|^4 + \zeta \sum_{n=1}^{N^{\rm rec}} k_n^2((p_n^{\rm rec})^2 + (q_n^{\rm rec})^2), \tag{3.12}$$

where d is the discretization step, $p_n^{\rm rec}$ and $q_n^{\rm rec}$ are the coefficients in formula (3.8), and the value of the weighting parameter $\zeta = 0.7$ has been chosen experimentally.

4. Numerical simulations.

4.1. Baseline example of transionospheric autofocus. In this example, we use the parabolic windowing function (2.8b) in (2.16) and take $F \equiv L_{\rm SA}/\Delta_{\rm A} = 100$, $\xi = 0.5$ in both (2.15) and (2.16). The discretization step for computing the numerical quadratures in (2.15) and

[6] Note that (2.15) and (2.16) represent stripmap processing for a one-dimensional image with no restriction on the value of ξ.

Table 1
Default coefficients in formula (3.5) for $\Psi(s)$ in Figure 3.

n	k_n	p_n	q_n
1	0.03770	-0.81357	5.98784
2	0.07540	-1.21312	0.90033
3	0.11310	0.64135	0.19871
4	0.15080	0.23489	-0.29575
5	0.18850	0.08524	0.22619
6	0.22619	-0.10959	-0.12715

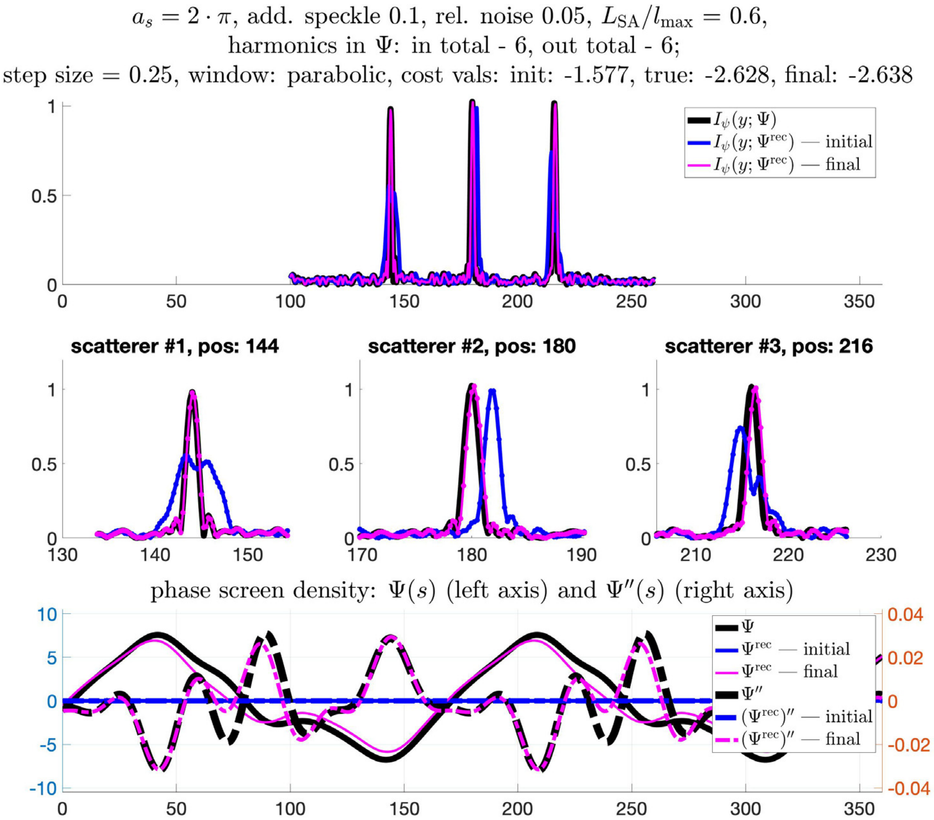

Figure 3. *Simultaneous reconstruction of Ψ and μ with the cost function (3.12) for $N = N^{\mathrm{rec}} = 6$.*

(2.16) (see also (3.12)) is $d = 1/4$. The scatterer model is given by (3.2b), (3.3) with $M = 3$, $z_1 = 144$, $z_2 = 180$, $z_3 = 216$, and $b_1 = b_2 = b_3 = 1$. The screen density function is described by formula (3.5) with $N = 6$ and the values of the parameters specified in Table 1. The values of k_n in Table 1 correspond to formula (3.6) while the values of p_n and q_n are obtained using a random number generator. Since the power spectrum of oscillations is rapidly decreasing [42, 51], adding higher harmonics has little effect on the quality of reconstructed images (see Appendix B for details).

Figure 3 illustrates the idea of optimization-based autofocus (3.4) and shows the reconstruction of both the reflectivity and phase screen density by minimizing the cost function

(3.12), with p_n^{rec} and q_n^{rec} being the optimization variables; see (3.8). In this example, the simulation and reconstruction wavenumber spectra (3.6) are identical, each containing six harmonics. However, the presence of both noise and clutter (see (3.2)) prevents the exact reconstruction of the "true" screen density Ψ. The top and bottom panels of Figure 3 present the one-dimensional image and the phase screen functions, respectively, while the plots in the middle row are zoom-ins to the peaks in the top panel. The minimization (3.4) is performed using an interior-point method implemented via the MATLAB `fmincon` function with an explicitly specified gradient of (3.12).

From Figure 3 we can see that although the level of distortions is high, the quality of the reconstructed image (purple curves), in terms of the height and shape of the peaks due to the point scatterers, is very close to that of the image reconstructed using the exact $\Psi(s)$ (black curves). Note also that $\Psi^{\text{rec}} = \Psi$ does not necessarily correspond to a stationary point of the cost functional in (3.12), so the values smaller than Cost$[\Psi]$ can be achieved, as is the case in Figure 3 (see the last line of the plot title).

4.2. Additional examples of reconstruction. In this section, we illustrate a variety of factors that affect the outcome of the focusing procedure, while a detailed analysis of those will be presented in the future.

4.2.1. Windowing function. Figure 4 demonstrates focusing with the rectangular window (2.8a) in (2.16). As expected, the peaks due to the point scatterers in this case appear narrower than those for the parabolic window [13]. However, we are going to see that the parabolic windowing function (2.8b) improves the autofocus behavior in more demanding settings.

4.2.2. The magnitude and horizontal scale of perturbations. When the magnitude of perturbations is large, the perturbations with a shorter horizontal scale cause a stronger

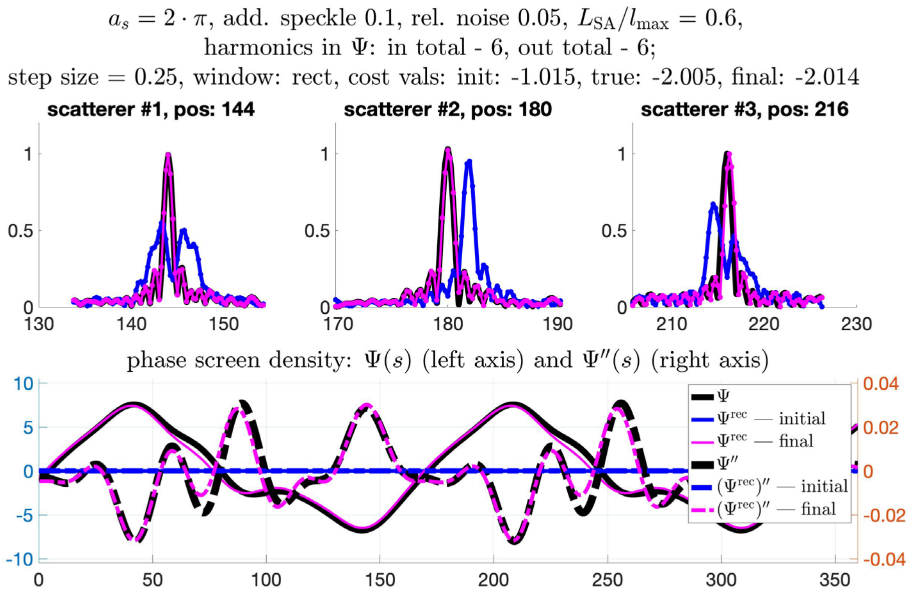

Figure 4. *Same as in Figure 3 but with a rectangular window.*

defocusing effect and thus may be expected to present a harder challenge for autofocus (see also [16, 19, 24]). We can observe this in Figure 5 where the heights of the peaks in the focused image are reduced quite noticeably, and the accuracy of reconstruction of Ψ is poor. When a rectangular window is used, these effects become stronger; see Figure 6.

Reconstruction with the magnitude a_s of (3.7) more than 3 times higher than that in the previous two cases is shown in Figures 7 and 8. Once again, we see that the parabolic window, unlike its rectangular counterpart, enables focusing for rather high levels of distortions.

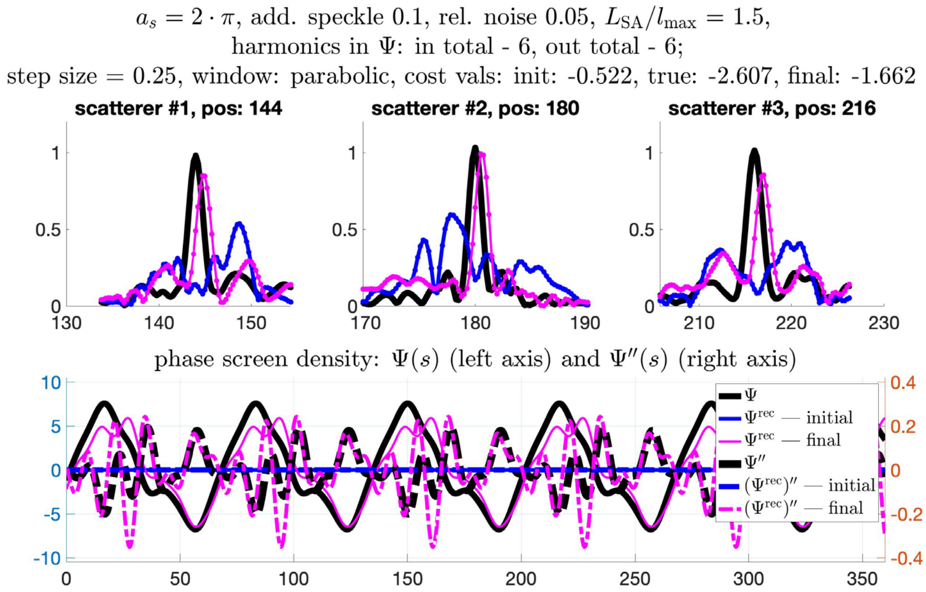

Figure 5. *Same as in Figure 3 but with a smaller value of* $l_{\max}$.

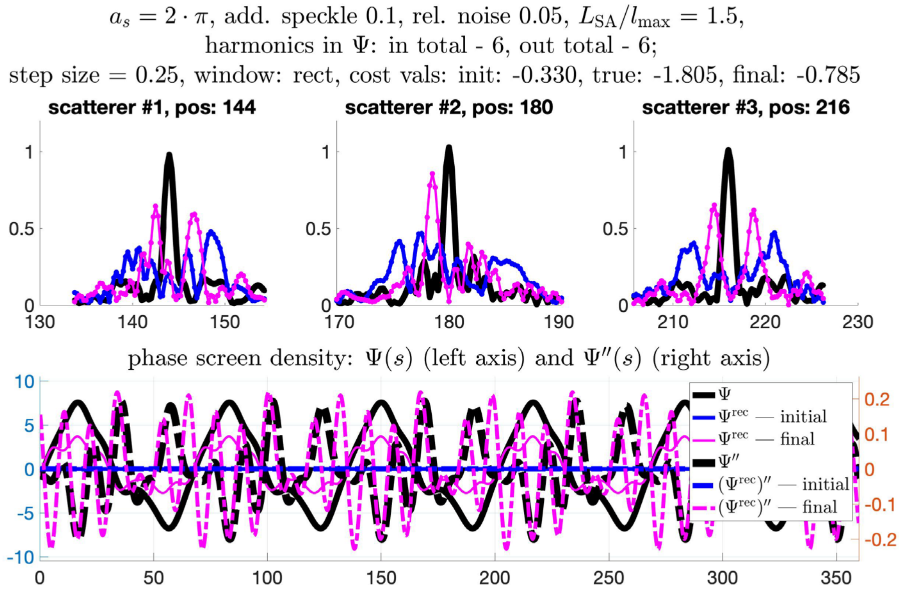

Figure 6. *Same as in Figure 5 but with a rectangular window.*

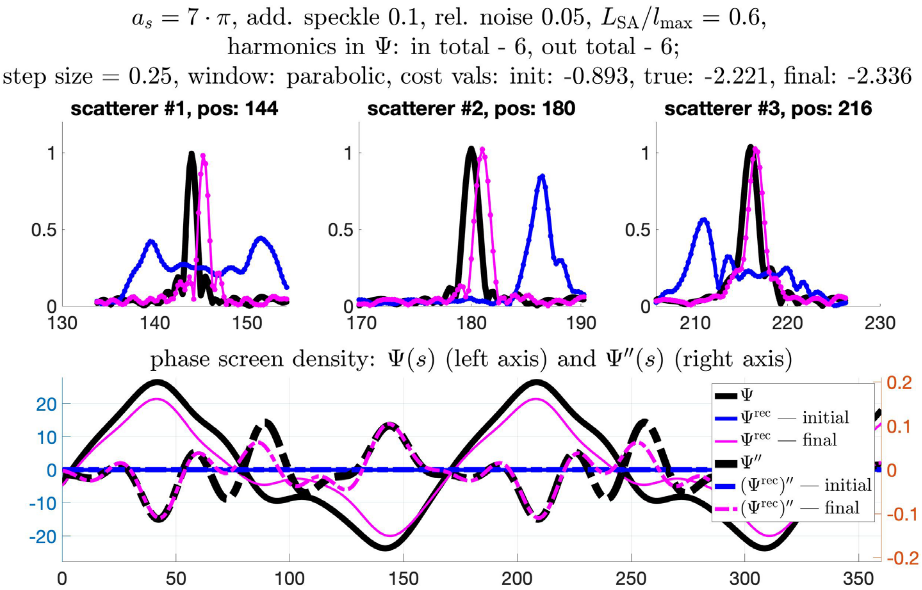

Figure 7. *Same as in Figure 3 but with a higher magnitude of perturbations; see (3.7).*

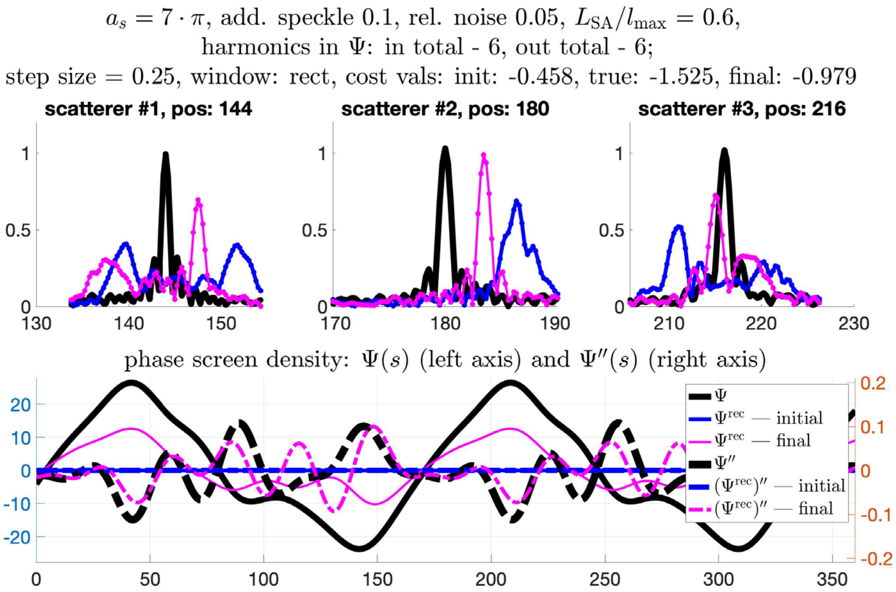

Figure 8. *Same as in Figure 7 but with a rectangular window.*

4.2.3. Nonperiodic perturbation function. According to (3.6), all wavenumbers in Table 1 are proportional to k_1. Therefore, the function $\Psi(s)$ in Figure 3, as well as several other figures, is periodic. However, condition (3.6) can be lifted, resulting in a nonperiodic realization of $\Psi(s)$; see Table 2 and Figure 10. Notice that although we choose $a_1 = 0$ for $\Psi(s)$ given by (3.5), this condition is not enforced in the spectrum of $\Psi^{\mathrm{rec}}(s)$.

Table 2
Coefficients in formula (3.5) for $\Psi(s)$ in Figure 10 (cf. Table 1).

n	k_n	p_n	q_n
1	0.03016	0.00000	0.00000
2	0.07157	-4.69435	3.48393
3	0.12161	1.93410	0.59926
4	0.17945	0.57836	-0.72820
5	0.24466	0.17641	0.46811
6	0.31702	-0.19452	-0.22570

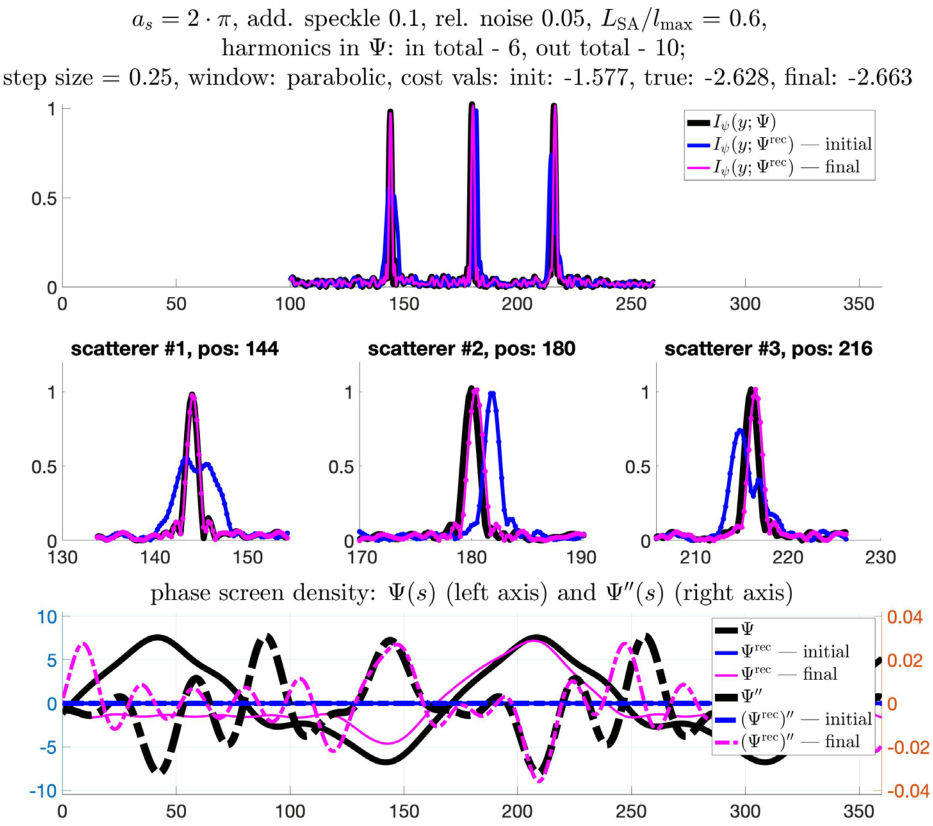

Figure 9. *Same as in Figure 3 but with with the wavenumbers $\{k_n^{\mathrm{rec}}\}$ different from $\{k_n\}$ (see (3.8)); namely, $k_1^{\mathrm{rec}} = 0.7k_1$ and $N^{\mathrm{rec}} = 10$ versus $N = 6$.*

In Figure 10, the shape of the peaks in the image is quite good (similar to Figure 3), yet the perturbation function is not reconstructed so well. We discuss this issue further in subsection 4.2.4.

4.2.4. Different wavenumber spectra for simulation and reconstruction. Figure 9 shows an example where the wavenumber spectra of the original and reconstructed phase screen density functions are different (see (3.5) and (3.8)), with $k_1^{\mathrm{rec}} = 0.7k_1$ and $N = 6$ versus $N^{\mathrm{rec}} = 10$.

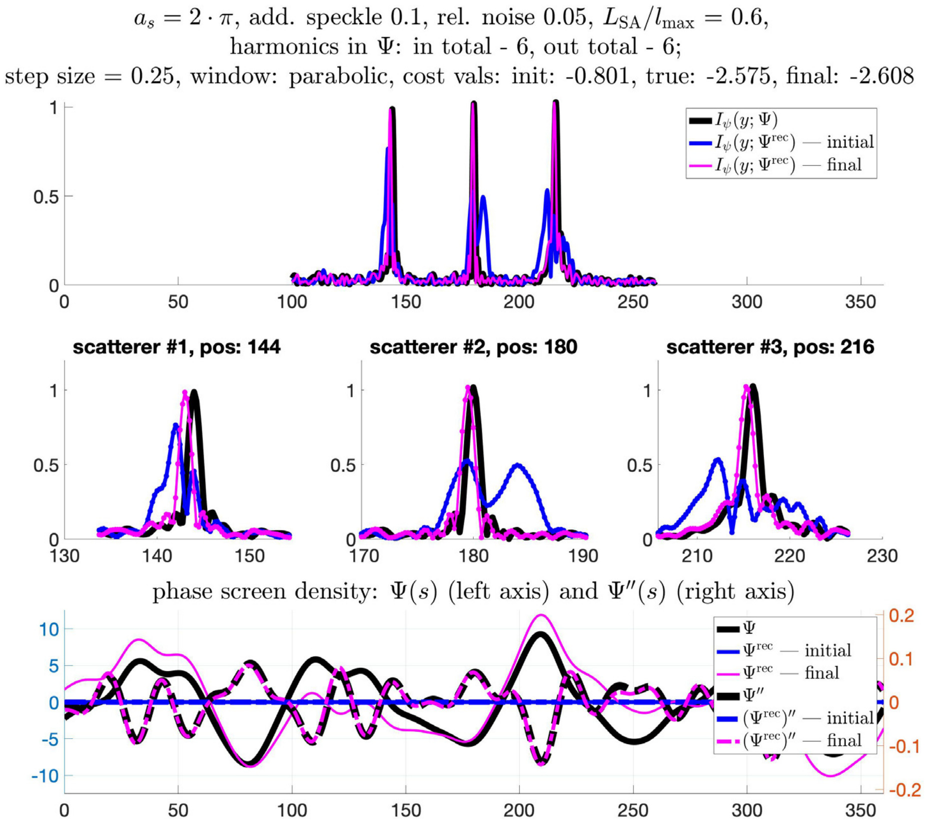

Figure 10. *Reconstruction of the scene with a nonperiodic $\Psi(s)$; see subsection 4.2.3.*

The quality of the reconstructed peaks suggests that the distortions are essentially compensated; however, it can be seen that the function Ψ itself is not reconstructed very accurately. The same is true about Figure 10.

We can offer the following interpretation to this observation. The cost function (3.11) favors sharp and high peaks [45]. At the same time, it is the second derivative of the phase perturbation that may cause a deterioration of the peak. Indeed, by considering the Taylor expansion for Ψ one can show that the constant term has no effect on the sharpness of the peaks in $|\mathcal{I}|$, while the linear term results in a horizontal shift of the peak without its deformation; see also [19, 24]. Hence, as the peaks in Figures 9 and 10 are sharp, we conclude that the second derivative of Ψ must have been reconstructed accurately in the region surrounding the peaks. Indeed, in the corresponding lower panels we can observe that $|(\Psi^{\mathrm{rec}})'' - \Psi''|$ is relatively small in the central part of the domain, while toward the endpoints it may increase.

Note that for $F = 100$ and $\xi = 0.5$ (see subsection 4.1), the peak due to a point scatterer located at z_m, $m = 1, 2, 3$, is affected by the values of $\Psi(s)$ and $\Psi^{\mathrm{rec}}(s)$ for

$$|s - z_m| \le \xi F/2 = 25; \tag{4.1}$$

see (1.1) and (2.5). For a group of point scatterers, the domain of dependence is given by

$$\min_m(z_m) - \xi F/2 \le s \le \max_m(z_m) + \xi F/2, \tag{4.2}$$

because the appearance of the peaks does not depend on the values of $\Psi^{\text{rec}}(s)$ outside of this domain. For our current setup, the interval (4.2) is $119 \leq s \leq 241$. A similar observation can be made about the area around the relatively well-reconstructed middle peak in Figure 8, where the domain of dependence given by (4.1) is $155 \leq s \leq 205$.

4.2.5. Multi-start initialization. Since the cost function (3.12) is a smooth function of the optimization variables p_n^{rec} and q_n^{rec} (see (3.8)), its minimization can be performed using gradient-based methods. Still, the outcome of the optimization procedure depends on the solver initialization. In all of our previous examples, the initial guess was zero: $\Psi^{\text{rec}} \equiv 0$, i.e., $p_n^{\text{rec}} = 0$ and $q_n^{\text{rec}} = 0$ for all n. By exploring the behavior of the cost function around the stopping points of the optimizer and comparing the results against $\text{Cost}[\Psi]$, we find that the cases of poor reconstruction, such as those shown in Figures 5, 6, and 8, correspond to local rather than global minima of the cost function.

One possible approach to finding the global minimum is to generate multiple starting points and choose the best minimization outcome. Our observations show that the optimization landscape for the problem of minimizing (3.12) may have multiple local minima. For the wavenumber spectrum and other parameters that correspond to Figure 5, we have created $K = 10$ realizations of Ψ and n_{compl} or, equivalently, $(\{\varphi_n\}, \mu_{\text{clutter}}, u_{\text{noise}})$:

$$(\{\varphi_n\}, \mu_{\text{clutter}}, u_{\text{noise}})_k, \quad k = 1, \dots, K; \tag{4.3}$$

see formulae (3.5), (3.9), and (3.10). Each triplet (4.3) gives rise to a realization of the phase screen $\Psi^{(k)}$ and observable radar field $u_{\text{observed}}^{(k)}$; see formulae (2.15) and (3.2). For each $u_{\text{observed}}^{(k)}$, $k = 1, \dots, K$, we have performed a gradient-based minimization of the cost function (3.12) starting from 600 randomly chosen initial guesses. Out of the 600 results, we have chosen the best one, i.e., the one with the minimum cost function. The corresponding reconstructed screen density is denoted by $\Psi_{\text{multi}}^{(k)}$, $k = 1, \dots, K$.

Moreover, for each $u_{\text{observed}}^{(k)}$, $k = 1, \dots, K$, we have performed a single optimization starting from the initial guess $\Psi^{\text{rec}} = 0$. The resulting reconstructed screen density is denoted by $\Psi_{\text{single}}^{(k)}$, $k = 1, \dots, K$. The corresponding image $\mathcal{I}(y, \Psi_{\text{single}}^{(k)})$ will serve as a reference point for comparison for each $k = 1, \dots, K$.

To assess the effect of multi-start on autofocus performance, we compare the height of the peaks in the images $\mathcal{I}(y, \Psi_{\text{multi}}^{(k)})$ and $\mathcal{I}(y, \Psi_{\text{single}}^{(k)})$, as well as the values of the cost function $\text{Cost}[\Psi_{\text{multi}}^{(k)}]$ and $\text{Cost}[\Psi_{\text{single}}^{(k)}]$ (see (3.12)), for $k = 1, \dots, K$. We also compute the similar metrics for the case of the exact reconstruction, i.e., where one uses $\Psi^{\text{rec}} = \Psi^{(k)}$ in formula (2.16) and obtains $\mathcal{I}(y, \Psi^{(k)})$, $k = 1, \dots, K$. (Exact reconstruction is an idealized scenario that requires no optimization and rather assumes that the phase correction is known.)

Accordingly, for each $k = 1, \dots, K$ and each of the three peaks we consider the variation (increase) in the peak height due to the multi-start,

$$\max_{y \text{ near peak}} |\mathcal{I}(y, \Psi_{\text{multi}}^{(k)})| - \max_{y \text{ near peak}} |\mathcal{I}(y, \Psi_{\text{single}}^{(k)})|, \tag{4.4a}$$

and the corresponding variation due to the exact reconstruction,

$$\max_{y \text{ near peak}} |\mathcal{I}(y, \Psi^{(k)})| - \max_{y \text{ near peak}} |\mathcal{I}(y, \Psi_{\text{single}}^{(k)})|. \tag{4.4b}$$

Table 3
The effect of multi-start on autofocus performance.

	Wavenumber spectra for Ψ and Ψ^{rec}					
	Identical				Different	
	Multi-start		$\Psi^{\text{rec}} = \Psi$		Multi-start	
	mean	std	mean	std	mean	std
Peak #1 height increase	0.0818	0.0933	0.0889	0.0935	0.0185	0.1497
Peak #2 height increase	0.0833	0.1035	0.0910	0.1011	0.0578	0.0887
Peak #3 height increase	0.0825	0.0828	0.0883	0.0825	0.1641	0.1400
Cost function decrease	0.5496	0.5268	0.5272	0.5242	0.4245	0.2026

We also consider the reduction in the value of the cost function (3.12) due to the multi-start,

$$\text{Cost}[\Psi^{(k)}_{\text{single}}] - \text{Cost}[\Psi^{(k)}_{\text{multi}}], \tag{4.4c}$$

and that due to the exact reconstruction,

$$\text{Cost}[\Psi^{(k)}_{\text{single}}] - \text{Cost}[\Psi^{(k)}]. \tag{4.4d}$$

Then, we compute the mean and standard deviation of each of the four quantities (4.4) over the ensemble $k = 1, \dots, K$, $K = 10$. The results are shown in columns 2–5 of Table 3.

In addition, we have performed the same experiment for the case where the wavenumber spectra for Ψ and Ψ^{rec} were different (namely, we used $N = 6$, $N^{\text{rec}} = 10$, and $k_1^{\text{rec}} = 0.7k_1$). In that case, the exact reconstruction $\Psi^{\text{rec}} = \Psi$ is not possible, and accordingly, we could only consider the gains in autofocus performance due to the multi-start (4.4a) and (4.4c), while the quantities (4.4b) and (4.4d) were not available. The mean and standard deviation of the quantities (4.4a) and (4.4c) in the case where the wavenumber spectra for Ψ and Ψ^{rec} were different are presented in columns 6 and 7 of Table 3.

From Table 3 we see that appreciable gains can be achieved by the multi-start method as compared to a single optimization run. With the typical peak height and cost value being 1 and -2, respectively (the cost values are listed in the last line of the plot title in Figure 3 and other similar figures), we find that on average, the relative increase in the peak height due to the multi-start is about 10%, whereas the relative decrease of the cost function value is about 20%. At least for the case of identical wavenumber spectra presented in Table 3, the multi-start approach is nearly as effective as the exact reconstruction of Ψ.

For the case of different wavenumber spectra, we plot the average error of reconstruction of the screen density function in Figure 11. As expected, we see that the accuracy of reconstruction is significantly higher inside the domain of dependence (4.2) (cf. Figure 9).

In addition, in Appendix C we analyze the case of resolving a pair of closely located point scatterers in the target area.

5. Discussion and future work.

We have developed and tested numerically an optimization-based autofocus algorithm for transionospheric SAR imaging. Its primary objective is to compensate for the distortions of SAR images due to turbulence in the Earth's ionosphere. The ionospheric turbulence is modeled with the help of a phase screen. The unknown ground

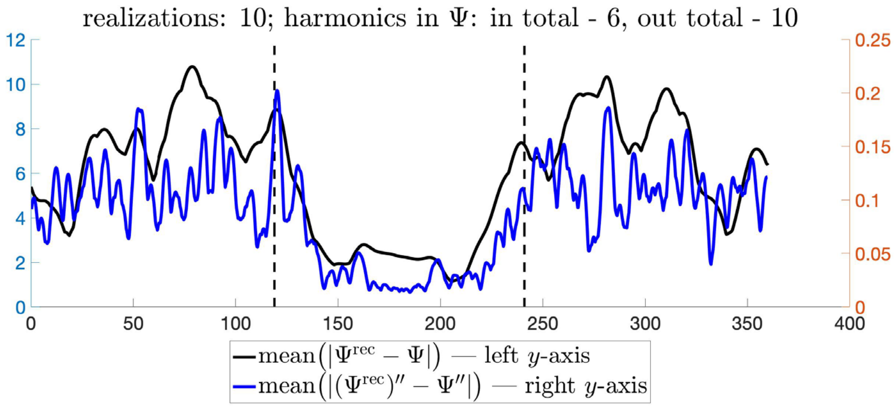

Figure 11. *Average accuracy of reconstruction of the phase screen density for the case of different wavenumber spectra. The boundaries of the domain of dependence* (4.2) *are marked by the vertical dashed lines.*

reflectivity is reconstructed by the conventional SAR signal processing that involves the application of a matched filter and summation along the synthetic array. Along with the SAR reconstruction, the proposed autofocus procedure determines the ionospheric phase correction using a variational approach. The best phase correction is the one that optimizes certain desired characteristics of the image, such as the sharpness of its peaks due to point scatterers.

The current paper reports on the initial stages of development of the proposed autofocus procedure. To illustrate its performance, we have conducted a set of numerical experiments with a limited number of realizations of the problem parameters. In our simulations, we varied the azimuthal windowing function, the magnitude and horizontal scale of perturbations, the wavenumber spectrum for the reconstructed screen density function, and the distance between point scatterers, and we also used multiple realizations of the screen density function with a fixed spectrum. In addition to these factors, the autofocus performance may also depend on

- the levels of noise and clutter; see (3.2), (3.9), and (3.10);
- the number of harmonics in the representation of Ψ and Ψ^{rec}; see (3.5) and (3.8);
- the length of the synthetic aperture $F = L_{\text{SA}}/\Delta_{\text{A}}$;
- the difference between the assumed and actual screen elevations; see [21].

Moreover, as the density of the phase screen depends on the set of random phases $\{\varphi_n\}$ (see formula (3.5)), the degree of distortions and efficiency of autofocus shall be evaluated in the corresponding stochastic framework. Specifically, multiple realizations of the phase screen, as well as noise and clutter, shall be considered, and the quality of reconstruction of both μ and Ψ shall be judged across the entire ensemble, similarly to subsection 4.2.5 and Appendix C. We will report on the results of this extended study in a subsequent publication.

The phase screen representation of the Earth's ionosphere that we employed in the current paper is quite common for the SAR community [1, 4, 40]. Sometimes, multiple phase screens are used [58], and our optimization procedure can be extended to handle those as well. However, a sufficient justification to support the use of the phase screens for the analysis of transionospheric SAR is lacking in the literature. Moreover, it is known that in general the phase screens are not always applicable [36].

The actual Earth's ionosphere has finite thickness. It is a layer of plasma that is nonuniform both vertically and horizontally [3, 18, 41]. Two different rays (signal travel paths) that intersect the screen at the same point will necessarily acquire the same phase perturbation. However, otherwise these rays may travel through different parts of the ionosphere. Therefore, in the full-fledged finite-thickness setting they will acquire different phase perturbations. The effect of the resulting mismatch on the autofocus performance needs to be analyzed.

An argument can be given, similar to the one in [18, Appendices 4.A.1 and 4.A.2], that even when the correlation length of turbulent fluctuations of the electron number density in the ionosphere is short, the phase perturbations will nonetheless be strongly correlated for the rays traveling through different parts of the ionosphere but crossing a given surface, the screen, at the same location. These correlation properties can, perhaps, justify the use of the phase screens for certain ionospheric conditions and certain SAR imaging regimes. For other ionospheric and/or SAR conditions, though, the possibility of using a finite-thickness representation of the ionosphere for the development of transionospheric autofocus will need to be explored. This group of issues with be the subject of our future work.

In addition, the following extensions of the work reported in this paper are worthwhile.

Our current analysis relies on having several dominant point scatterers in the target area. The focusing ability of the proposed methodology should also be investigated in the case where the target contains no point scatterers. The following formulation for reflectivity of a distributed target [47] may be considered as a replacement for (3.3):

$$\mu_{\text{target}}(z) = g(z) \cdot n_{\text{compl}}, \quad \text{where} \quad g(z) \geq 0, \quad \left|\frac{\mathrm{d}g}{\mathrm{d}z}\right| \ll \frac{g}{\Delta_{\mathrm{A}}};$$

cf. (3.10). For this scatterer model, the goal of the reconstruction is to retrieve the modulating function $g(z)$. A study of the optimization-based conventional SAR autofocus (i.e., the case of $\xi = 1$) that included distributed targets can be found in [15].

Even if the scene contains dominant point scatterers, the autofocus performance may depend on the number of such bright points. As this number grows, the relative cost of "losing" one scatterer decreases, and individual scatterers located far from the groups of other scatterers appear more vulnerable than others. This effect may also depend on the chosen cost function and parameterization of the phase screen density. Overall, a study of this topic may be worthy of a separate publication.

We have seen that by using a parabolic windowing function (2.8b) in (2.15), we improve the focusing performance. Other types of windows, such as the popular Hann, Hamming, or Kaiser windows [32], can also be tried. In general, such windows are known to suppress the oscillations of the point spread function (PSF). Hence, studying the various approaches to regularization of $\mathcal{I}$ and its effect on autofocus is of interest.

The advantage of Fourier representation of the phase screen density (see (3.5)) is that the relevant scales of turbulence are specified explicitly via the wavenumber spectrum $\{k_n\}$. Yet the Fourier representation (3.5) offers no localization with respect to the space variable s. This may be seen as a drawback because there is no easy way to improve a "partially focused" image, such as that in Figure 7, where the middle peak is sharp whereas two others are not. Representation of $\Psi(s)$ by splines may be considered a viable alternative, while the control of the horizontal scales can be rendered by introducing a penalty term into the cost function.

When discussing the role of the second derivative of Ψ in subsection 4.2.4, we have indicated that the constant and linear terms in the Taylor expansion of Ψ have no effect on the image sharpness and, hence, the cost function. Accordingly, each minimum of the cost function (either local or global) may be attained by an entire class of screen densities. Removing this ambiguity may improve the performance of the optimizer.

The presence of local minima in the autofocus optimization problem (3.4) is demonstrated by the results shown in Figures 5, 6, and 8. We see that local minima lead to poor focusing. Convexification of the problem is desirable (see, e.g., [28]); however, no efficient convexification technique could be found for (2.16). In the absence of a convex metric (see also the discussion about metrics towards the end of subsection 3.2), the multi-start approach (subsection 4.2.5) may improve the results. Alternatively, one can explore such techniques as genetic algorithms or swarm optimization [38]. Similar to multi-start, these methods are computationally expensive. Another difficulty is that the values of some key parameters, such as the number of starting points or particles in the swarm, should be found experimentally because little is known about the "basins of attraction" of the local and global minima in multidimensional spaces; see, e.g., [62].

Arguably, the large differences between the values at the local and global minima in Figures 5, 6, and 8 indicate that the genetic- and swarm-based methods may have an advantage over the multi-start approach. For example, in the swarm optimization, the particle near the local minimum can be pulled away from the corresponding attraction basin once the difference between the cost function value at the particle's coordinate and the current population minimum becomes large enough [38]. This leads to a more efficient utilization of computational resources as compared to the multi-start, where "the particle" remains stuck at this local minimum. For the same reason, when budgeting multi-start computations, increasing the number of initial guesses should be preferred to strengthening the stopping criteria of the gradient-based optimizer.

An extension of (2.15) and (2.16) to the case of the two-dimensional targets and images (with both azimuthal and range coordinates present) will provide the additional data for focusing and allow one to properly take into account the phenomena of range cell migration and textured clutter [13, 21, 47].

Appendix A. Variance of the perturbation phase and $\mathrm{C_kL}$. A brief and very helpful presentation of the concept and meaning of $\mathrm{C_kL}$ as a measure of the ionospheric scintillation can be found in [42, formulae (4)–(6)]. In order to calculate the $\mathrm{C_kL}$ value corresponding to the magnitude of $\Psi(s)$ in Figure 2, we used the following relation (see [51, formula (19)]):

$$\langle \Psi^2 \rangle = 2 r_{\mathrm{e}}^2 \lambda^2 \frac{H}{\cos\theta} G C_s \left(\frac{2\pi}{r_0}\right)^{-2\mathrm{v}+1} \frac{\Gamma(\mathrm{v}-1/2)}{4\pi\Gamma(\mathrm{v}+1/2)}. \tag{A.1}$$

In this formula, the factor 2 is due to the two-way propagation, r_{e} is the classical electron radius, λ is the radar wavelength, H is the thickness of the plasma layer, θ is the incidence angle, and G is the geometric factor that will be ignored (i.e., $G=1$). Further, C_s is the factor in the formula defining the spectral density function of fluctuations of the electron number density n_{e}:

$$Q(K) = \frac{C_s}{\left((2\pi/r_0)^2 + K^2\right)^{\mathrm{v}+1/2}},$$

such that

$$\langle (n_{\mathrm{e}} - \langle n_{\mathrm{e}} \rangle)^2 \rangle = \int_0^\infty 4\pi K^2 Q(K)\, \mathrm{d}K.$$

In turn, the parameters v and r_0 are called the spectral index and the outer scale of the ionospheric turbulence; following [42], we specify their values as $\mathrm{v} = 3$ and $r_0 = 5km$, respectively.

The parameter $\mathrm{C_kL}$ is defined as the intensity of the electron number density pulsations integrated over the plasma layer and scaled with the wavenumber $K_{1km} = 2\pi/(1km)$:

$$\mathrm{C_kL} = C_s H K_{1km}^{-(2\mathrm{v}+1)}. \tag{A.2}$$

The units of $\mathrm{C_kL}$, almost universally dropped in the literature, are $[m^{-2}]$. The estimate of the value of $\mathrm{C_kL}$ for Figure 2 in the main text has been obtained by substituting the magnitude of $\Psi(s)$ and the radar parameters from [18, Table 1.1] into (A.1) and (A.2). The resulting value of $\mathrm{C_kL} \sim 10^{32}\, m^{-2}$ is relatively high; see, e.g., [55]. Yet we can find the values of $\mathrm{C_kL}$ orders of magnitude higher that have been reported in the literature and used in the context of transionospheric SAR imaging; see [7, 25, 42, 50].

Appendix B. Reconstruction with a reduced number of harmonics. In the simulations reported in this work we used fewer than 10 harmonics in the spectrum, resulting in $k_N/k_1 < 10$; see (3.5) and (3.6). It is therefore a legitimate concern whether the simulations with such a spectrum are representative of focusing with a real ionosphere where the scales may range from a few kilometers down to about $70m$ (see, e.g., [14, 42, 61]).

Nevertheless, we find that adding harmonics with larger wavenumbers to the simulation has little effect on the quality of reconstructed images. The reason is that the power spectrum of oscillations decreases rapidly toward smaller scales; see [51]. This conclusion is supported by a series of reconstructions that we have performed; see Figure 12. For the simulations

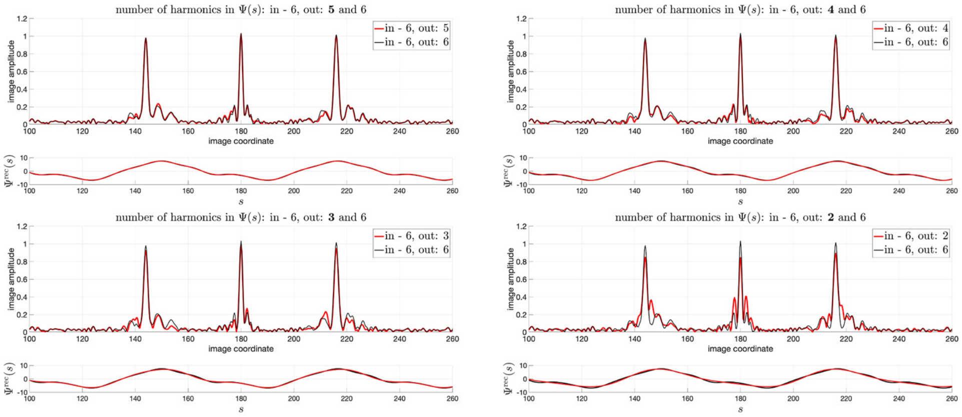

Figure 12. *Reconstruction with a reduced number of harmonics. The number of "in" and "out" harmonics corresponds to the representation of $\Psi(s)$ and $\Psi^{\mathrm{rec}}(s)$ via (3.5) in (2.15) and (2.16), respectively.*

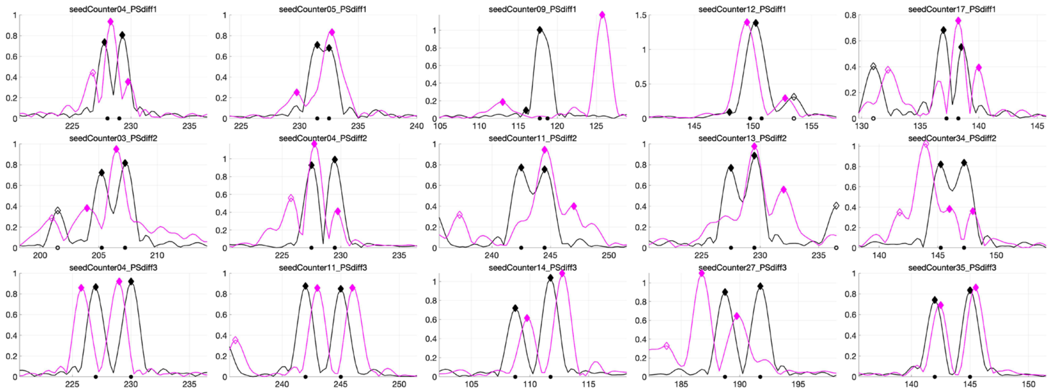

Figure 13. *Examples of focusing results for scenes containing a pair of closely located point scatterers. The spacing in the pair is* 1 *(top row),* 2 *(middle row), and* 3 *(bottom row). The black and purple curves correspond to the reconstruction with* $\Psi^{\mathrm{rec}} = \Psi$ *and* Ψ^{rec} *resulting from the optimization with the cost function* (3.12)*, respectively. The black dots on the abscissa axis correspond to the "true" location of the scatterers in the pair, whereas the locations of the auxiliary point scatterers are marked by the black hollow circles. The filled diamonds indicate the detected peaks due to the pair of scatterers, whereas the contoured diamonds correspond to the additional peaks.*

illustrated by Figure 12, $\Psi^{\mathrm{rec}}(s)$ in formula (2.16) is obtained by dropping one or more of the shortest harmonics from $\Psi(s)$, and the resulting image is compared with the one built with the original Ψ. We observe that with 6 harmonics in the spectrum of Ψ as in Table 1, the quality of the images obtained using 5 or even 4 longest harmonics in the spectrum of Ψ^{rec} is quite satisfactory for the chosen class of targets.

Appendix C. Resolving a pair of closely located point scatterers. We reconstruct the scenes that contain a pair of point scatterers at a certain distance from each other, henceforth called the PS-spacing. The goal is to see how accurately this scene is represented in the resulting image. In our experiments, we varied the value of PS-spacing from 1 to 12 in resolution units; see subsection 2.3. For each value of PS-spacing, we have conducted 30 individual reconstruction experiments. The reconstruction examples are illustrated in Figures 13 and 14, whereas the averaged metrics characterizing the distortions in the appearance of the pair of point scatterers are plotted in Figures 15 and 16.

In the said experiments, the radar parameters, as well as the clutter and noise levels, were the same as in Figure 3. The magnitudes of the point scatterers in the pair are uniformly distributed in the range between 0.7 and 1, and the position of the midpoint of the pair is random. In addition to the pair, four more point scatterers, with the magnitudes ranging from 0.3 to 0.5, have been randomly placed in the imaged scene such that none of them gets closer than PS-spacing to any scatterer in the pair. The phases of the scatterers are uniformly random in $[0, 2\pi)$. For each realization of μ_{target} obtained this way (see (3.2b)), we generate separate random realizations of u_{noise}, μ_{clutter}, and $\{\varphi_n\}$ (see (3.9), (3.10), and (3.5), respectively). The optimization procedure is then applied to each of the 30 data vectors u_{observed} (see (3.2a)) for each PS-spacing, and the results are analyzed as follows.

The top row in Figure 13 shows clips from the images where the value of PS-spacing is 1 (the entire images can be found in Figure 14). We see that even with a perfect reconstruction of

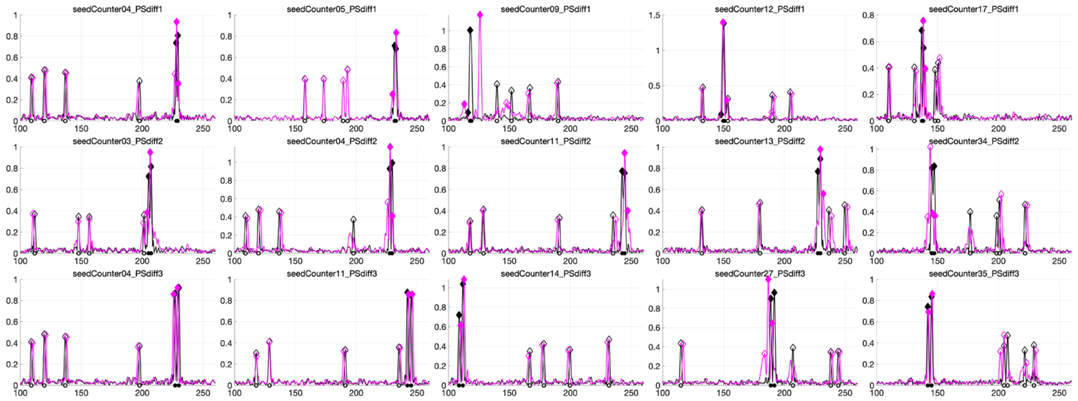

Figure 14. *Same as in Figure 13, but showing the entire scenes.*

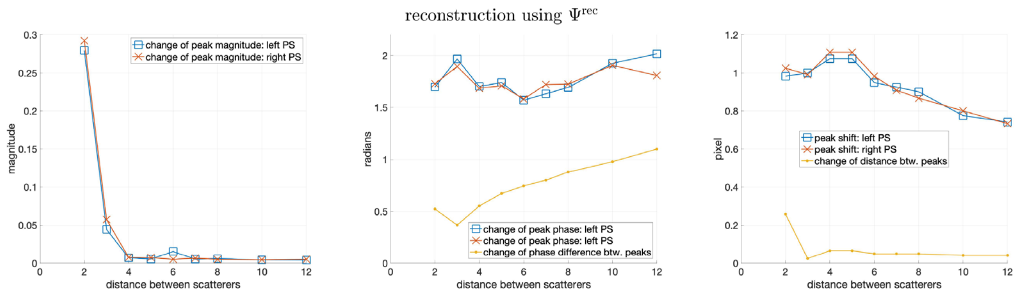

Figure 15. *Averaged distortion measures for a pair of close point scatterers for the reconstruction with* Ψ^{rec} *resulting from the optimization with the cost function* (3.12).

the phase perturbation, i.e., $\Psi^{\text{rec}} = \Psi$ (black curves), the two peaks don't always separate from each other. For the middle row, where PS-spacing equals 2, the perfect reconstruction provides a certain degree of peak separation in all demonstrated cases, whereas the optimization-based reconstruction (purple curves) fails to do so most of the time. However, for PS-spacing = 3 (the bottom row), the minimization-based reconstruction is shown to produce a pair of well-defined peaks with the magnitudes and locations close to those obtained using the perfect reconstruction. The same is true for higher values of PS-spacing as well.

To characterize the autofocus performance quantitatively in the case of a pair of peaks, we formulate the distortion metrics as follows. In the sampled images, 6 highest peaks are determined using the MATLAB `findpeaks` function (see [39]), and two peaks with the locations closest to the midpoint between the original coordinates of the scatterers are selected as those representing the pair. Using the peak location and value, i.e., y_j and $\mathcal{I}(y_j)$, we calculate the absolute changes of the peak magnitude, complex phase, and location (the left, central, and right panels in Figure 15, respectively) with respect to the corresponding parameters of the point scatterer, i.e., (b_m, z_m) in (3.3), and average the results over 30 realizations for each value of PS-spacing. These averages are plotted against the value of PS-spacing for the optimization-based reconstruction and perfect reconstruction in Figures 15 and 16, respectively. Since the distortion metrics for PS-spacing = 1 come out disproportionally high, this data point is excluded from the plots.

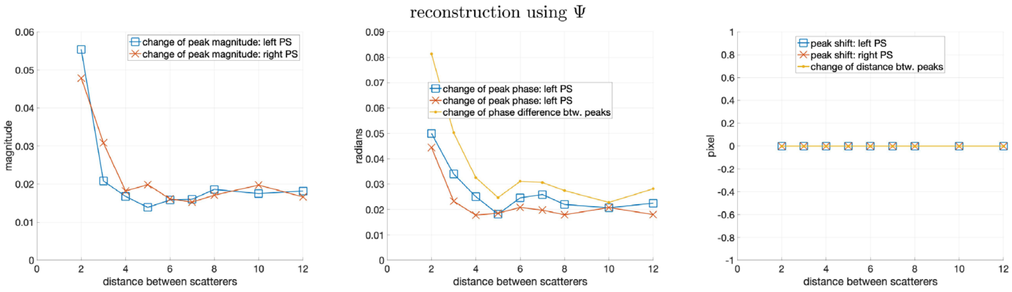

Figure 16. *Same as in Figure 15, but for* $\Psi^{\text{rec}} = \Psi$.

From Figure 15, we can see that starting from the actual PS-spacing = 4, the distortions in the peak magnitude and PS-spacing calculated from the image are low; see the left panel and the yellow curve on the right panel, respectively. The distortions in the peak phases (the middle panel) remain comparatively high. The latter is not surprising because the cost function is not sensitive to the image phase. We can also see that the distortions in the absolute peak locations (the right panel) are significantly higher that those in the PS-spacing. A part of the explanation is, again, the lack of sensitivity of the cost function (3.12) to the shift of the image as a whole. Besides, note that this shift is proportional to the gradient of the residual phase perturbations, i.e., $(\Psi - \Psi^{\text{rec}})'$. As long as the value of PS-spacing is small compared to the horizontal scale of phase perturbation (cf. (2.14)), the change in PS-spacing should be proportional to the second derivative of the residual phase perturbation, i.e., $(\Psi - \Psi^{\text{rec}})''$. Per the discussion regarding Figure 9 in the beginning of subsection 4.2.4, we expect that with a good focusing, the latter expression will be small.

A comparison between Figures 15 and 16 shows that the perfect reconstruction yields much smaller position and phase errors as compared to the optimization-based approach, whereas the results regarding the peak amplitudes are comparable. This observation is consistent with the formulation of the cost function in (3.12).

Acknowledgment. We would like to thank the anonymous referees for their comments and suggestions.

REFERENCES

[1] D. P. Belcher, *Theoretical limits on SAR imposed by the ionosphere*, IET Radar Sonar & Navigation, 2 (2008), pp. 435–448, https://doi.org/10.1049/iet-rsn:20070188.

[2] D. P. Belcher and N. C. Rogers, *Theory and simulation of ionospheric effects on synthetic aperture radar*, IET Radar Sonar & Navigation, 3 (2009), pp. 541–551, https://doi.org/10.1049/iet-rsn.2008.0205.

[3] N. Blaunstein and E. Plohotniuc, *Ionosphere and Applied Aspects of Radio Communication and Radar*, CRC Press/Taylor & Francis, Boca Raton, FL, 2008.

[4] R. Brcic, A. Parizzi, M. Eineder, R. Bamler, and F. Meyer, *Estimation and compensation of ionospheric delay for SAR interferometry*, in Proceedings of the 2010 IEEE International Geoscience and Remote Sensing Symposium (IGARSS'10), Honolulu, Hawaii, IEEE, 2010, pp. 2908–2911.

[5] R. Brcic, A. Parizzi, M. Eineder, R. Bamler, and F. Meyer, *Ionospheric effects in SAR interferometry: An analysis and comparison of methods for their estimation*, in Proceedings of the 2011

IEEE International Geoscience and Remote Sensing Symposium (IGARSS'11), Vancouver, Canada, IEEE, 2011, pp. 1497–1500.

[6] M. Carbillet and A. Riccardi, *Numerical modeling of atmospherically perturbed phase screens: New solutions for classical fast Fourier transform and Zernike methods*, Appl. Optics, 49 (2010), pp. G47–G52.

[7] C. S. Carrano, K. M. Groves, and R. G. Caton, *Simulating the impacts of ionospheric scintillation on L band SAR image formation*, Radio Sci., 47 (2012), pp. 1–14.

[8] M. Charnotskii, *Sparse spectrum model for a turbulent phase*, J. Optim. Soc. Amer. A, 30 (2013), pp. 479–488.

[9] J. Chen, M. Xing, H. Yu, B. Liang, J. Peng, and G.-C. Sun, *Motion compensation/autofocus in airborne synthetic aperture radar: A review*, IEEE Geosci. Remote Sens. Mag., 10 (2021), pp. 185–206.

[10] M. Cheney, *A mathematical tutorial on synthetic aperture radar*, SIAM Rev., 43 (2001), pp. 301–312, https://doi.org/10.1137/S0036144500368859.

[11] M. Cheney and B. Borden, *Fundamentals of Radar Imaging*, CBMS-NSF Regional Conf. Ser. in Appl. Math. 79, SIAM, Philadelphia, 2009, https://doi.org/10.1137/1.9780898719291.

[12] D. Colton and R. Kress, *Inverse Acoustic and Electromagnetic Scattering Theory*, Appl. Math. Sci. 93, 3rd ed., Springer, New York, 2013, https://doi.org/10.1007/978-1-4614-4942-3.

[13] I. G. Cumming and F. H. Wong, *Digital Processing of Synthetic Aperture Radar Data*, Algorithms and Implementation, Artech House, Boston, 2005.

[14] P. Dyson, J. McClure, and W. Hanson, *In situ measurements of the spectral characteristics of F region ionospheric irregularities*, J. Geophys. Res., 79 (1974), pp. 1497–1502.

[15] J. Fienup and J. Miller, *Aberration correction by maximizing generalized sharpness metrics*, J. Optim. Soc. Amer. A, 20 (2003), pp. 609–620.

[16] J. Garnier and K. Sølna, *A multiscale approach to synthetic aperture radar in dispersive random media*, Inverse Problems, 29 (2013), 054006.

[17] M. Gilman, E. Smith, and S. Tsynkov, *Reduction of ionospheric distortions for spaceborne synthetic aperture radar with the help of image registration*, Inverse Problems, 29 (2013), 054005, https://doi.org/10.1088/0266-5611/29/5/054005.

[18] M. Gilman, E. Smith, and S. Tsynkov, *Transionospheric Synthetic Aperture Imaging*, Appl. Numer. Harmon. Anal., Birkhäuser/Springer, Cham, Switzerland, 2017, https://doi.org/10.1007/978-3-319-52127-5.

[19] M. Gilman and S. Tsynkov, *Mathematical analysis of SAR imaging through a turbulent ionosphere*, in Application of Mathematics in Technical and Natural Sciences: 9th International Conference for Promoting the Application of Mathematics in Technical and Natural Sciences—AMiTaNS'17, M. D. Todorov, ed., American Institute of Physics (AIP), 2017, 020003, https://doi.org/10.1063/1.5007357.

[20] M. Gilman and S. Tsynkov, *A mathematical perspective on radar interferometry*, Inverse Probl. Imaging, 16 (2022), pp. 119–152, https://doi.org/10.3934/ipi.2021043.

[21] M. Gilman and S. Tsynkov, *Vertical autofocus for the phase screen in a turbulent ionosphere*, Inverse Problems, 39 (2023), 045001, https://doi.org/10.1088/1361-6420/acb8d6.

[22] A. Glindemann, R. Lane, and J. Dainty, *Simulation of time-evolving speckle patterns using Kolmogorov statistics*, J. Mod. Optic., 40 (1993), pp. 2381–2388.

[23] V. Gracheva, J. S. Kim, P. Prats-Iraola, R. Scheiber, and M. Rodriguez-Cassola, *Combined estimation of ionospheric effects in SAR images exploiting Faraday rotation and autofocus*, IEEE Geosci. Remote Sens. Lett., 19 (2021), 8018705.

[24] C. V. Jakowatz, D. E. Wahl, P. H. Eichel, D. C. Ghiglia, and P. A. Thompson, *Spotlight-Mode Synthetic Aperture Radar: A Signal Processing Approach*, Springer, New York, 1996.

[25] Y. Ji, C. Yu, Q. Zhang, Z. Dong, Y. Zhang, and Y. Wang, *An ionospheric phase screen projection method of phase gradient autofocus in spaceborne SAR*, IEEE Geosci. Remote Sens. Lett., 19 (2022), 4504205.

[26] J. S. Kim, A. Danklmayer, and K. Papathanassiou, *Correction of ionospheric distortions in low frequency interferometric SAR data*, in Proceedings of the 2011 IEEE International Geoscience and Remote Sensing Symposium (IGARSS'11), IEEE, 2011, pp. 1505–1508.

[27] J. S. Kim, K. P. Papathanassiou, R. Scheiber, and S. Quegan, *Correcting distortion of polarimetric SAR data induced by ionospheric scintillation*, IEEE Trans. Geosci. Remote Sens., 53 (2015), pp. 6319–6335.

[28] M. V. Klibanov and J. Li, *Inverse Problems and Carleman Estimates—Global Uniqueness, Global Convergence and Experimental Data*, Inverse and Ill-posed Problems Ser. 63, De Gruyter, Berlin, 2021, https://doi.org/10.1515/9783110745481.

[29] D. L. Knepp and K. M. Groves, *The effect of ionospheric scintillation on phase gradient autofocus processing of synthetic aperture radar*, in 2013 7th European Conference on Antennas and Propagation (EuCAP), IEEE, 2013, pp. 3664–3667.

[30] J. Kolman, *PACE: An autofocus algorithm for SAR*, in IEEE International Radar Conference, IEEE, 2005, pp. 310–314.

[31] T. J. Kragh, *Minimum-entropy autofocus for three-dimensional SAR imaging*, in Algorithms for Synthetic Aperture Radar Imagery XVI, Proc. Vol. 7337, SPIE, 2009, pp. 93–103.

[32] N. Levanon and E. Mozeson, *Radar Signals*, John Wiley & Sons, Hoboken, NJ, 2004.

[33] Y. Li and S. O'Young, *Kalman filter disciplined phase gradient autofocus for stripmap SAR*, IEEE Trans. Geosci. Remote Sens., 58 (2020), pp. 6298–6308.

[34] Z. Li, S. Quegan, J. Chen, and N. C. Rogers, *Performance analysis of phase gradient autofocus for compensating ionospheric phase scintillation in BIOMASS P-band SAR data*, IEEE Geosci. Remote Sens. Lett., 12 (2015), pp. 1367–1371.

[35] K.-H. Liu, A. Wiesel, and D. C. Munson, *Synthetic aperture radar autofocus based on a bilinear model*, IEEE Trans. Image Process., 21 (2012), pp. 2735–2746.

[36] A. Mahalov and A. McDaniel, *Long-range propagation through inhomogeneous turbulent atmosphere: Analysis beyond phase screens*, Phys. Scripta, 94 (2019), 34003.

[37] P. A. Makarov, *Two-dimensional autofocus technique based on spatial frequency domain fragmentation*, IEEE Trans. Image Process., 29 (2020), pp. 6006–6016.

[38] *MATLAB Global Optimization Toolbox*, The MathWorks, Natick, MA, 2021.

[39] *MATLAB Signal Processing Toolbox*, The MathWorks, Natick, MA, 2021.

[40] K. E. Mattar and A. L. Gray, *Reducing ionospheric electron density errors in satellite radar interferometry applications*, Can. J. Remote Sens., 28 (2002), pp. 593–600.

[41] F. J. Meyer, *Performance requirements for ionospheric correction of low-frequency SAR data*, IEEE Trans. Geosci. Remote Sens., 49 (2011), pp. 3694–3702, https://doi.org/10.1109/TGRS.2011.2146786.

[42] F. J. Meyer, K. Chotoo, S. D. Chotoo, B. D. Huxtable, and C. S. Carrano, *The influence of equatorial scintillation on L-band SAR image quality and phase*, IEEE Trans. Geosci. Remote Sens., 54 (2016), pp. 869–880.

[43] A. Moreira, P. Prats-Iraola, M. Younis, G. Krieger, I. Hajnsek, and K. P. Papathanassiou, *A tutorial on synthetic aperture radar*, IEEE Geosci. Remote Sens. Mag., 1 (2013), pp. 6–43.

[44] R. L. Morrison, M. N. Do, and D. C. Munson, *SAR image autofocus by sharpness optimization: A theoretical study*, IEEE Trans. Image Process., 16 (2007), pp. 2309–2321.

[45] R. A. Muller and A. Buffington, *Real-time correction of atmospherically degraded telescope images through image sharpening*, J. Optim. Soc. Amer., 64 (1974), pp. 1200–1210.

[46] I. Naeh and A. Katzir, *Perfectly correlated phase screen realization using sparse spectrum harmonic augmentation*, Appl. Optics, 53 (2014), pp. 6168–6174.

[47] C. Oliver and S. Quegan, *Understanding Synthetic Aperture Radar Images*, Artech House Remote Sensing Library, Artech House, Boston, MA, 1998.

[48] P. Prats, A. Reigber, and J. J. Mallorqui, *Interpolation-free coregistration and phase-correction of airborne SAR interferograms*, IEEE Geosci. Remote Sens. Lett., 1 (2004), pp. 188–191.

[49] P. Prats, A. Reigber, and J. J. Mallorqui, *Topography-dependent motion compensation for repeat-pass interferometric SAR systems*, IEEE Geosci. Remote Sens. Lett., 2 (2005), pp. 206–210.

[50] G. Reeves, T. J. Colvin, and J. Locke, *Next Step Space Weather Benchmarks*, IDA Group Report NS GR-10982, Institute for Defense Analyses, Science & Technology Policy Institute, Washington, DC, 2019, https://www.ida.org/-/media/feature/publications/n/ne/next-step-space-weather-benchmarks/gr-10982.ashx.

[51] C. Rino, *A power law phase screen model for ionospheric scintillation:* 1. *Weak scatter*, Radio Sci., 14 (1979), pp. 1135–1145.

[52] C. Rino, *The Theory of Scintillation with Applications in Remote Sensing*, John Wiley & Sons, Hoboken, NJ, 2011.
[53] P. A. Rosen, S. Hensley, and C. Chen, *Measurement and mitigation of the ionosphere in L-band interferometric SAR data*, in Proceedings of the IEEE International Radar Conference, Arlington, VA, 2010, pp. 1459–1463.
[54] T. Scarnati and A. Gelb, *Joint image formation and two-dimensional autofocusing for synthetic aperture radar data*, J. Comput. Phys., 374 (2018), pp. 803–821, https://doi.org/10.1016/j.jcp.2018.07.059.
[55] J. A. Secan and R. M. Bussey, *An Improved Model of High-Latitude f-Region Scintillation (wbmod version* 13*)*, Technical report, Northwest Research Associates, Bellevue, WA, 1994.
[56] E. M. Smith and S. V. Tsynkov, *Dual carrier probing for spaceborne SAR imaging*, SIAM J. Imaging Sci., 4 (2011), pp. 501–542, https://doi.org/10.1137/10078325X.
[57] M. Suppa, *TerraSAR-X Image Product Guide*, Technical report, Airbus Intelligence, 2015, https://www.intelligence-airbusds.com/files/pmedia/public/r459_9_20171004_tsxx-airbusds-ma-0009_tsx-productguide_i2.01.pdf.
[58] A. E. Tippie and J. R. Fienup, *Phase-error correction for multiple planes using a sharpness metric*, Opt. Lett., 34 (2009), pp. 701–703.
[59] S. V. Tsynkov, *On SAR imaging through the Earth's ionosphere*, SIAM J. Imaging Sci., 2 (2009), pp. 140–182, https://doi.org/10.1137/080721509.
[60] C. R. Vogel, *Computational Methods for Inverse Problems*, Frontiers Appl. Math. 23, SIAM, Philadelphia, 2002, https://doi.org/10.1137/1.9780898717570.
[61] K. Yeh and C. Liu, *Diagnosis of the turbulent state of ionospheric plasma by propagation methods*, Radio Sci., 12 (1977), pp. 1031–1034.
[62] Y. Zhang and S. H. Strogatz, *Basins with tentacles*, Phys. Rev. Lett., 127 (2021), 194101.
[63] X. X. Zhu and R. Bamler, *Let's do the time warp: Multicomponent nonlinear motion estimation in differential SAR tomography*, IEEE Geosci. Remote Sens. Lett., 8 (2011), pp. 735–739.